

POLITECNICO DI TORINO

Master of Science in Aerospace Engineering

Master Thesis

**Sliding Mode Techniques and  
Dynamic Obstacle Avoidance for  
Rendezvous Maneuver**



*Supervisor:*

Dr. Elisa Capello

*Co-supervisor:*

Dr. Elisabetta Punta

*Candidate:*

Mauro Mancini

236019

March 2019



# Abstract

The purpose of this thesis is to demonstrate the effectiveness of the artificial potential field (APF) method to bypass obstacles in orbital maneuvers. In particular, the study is applied to a rendezvous maneuver, in which a moving satellite (Chaser) is trying to reach a second satellite (Target). In this thesis, a fixed Target is considered, furthermore both position and attitude dynamics is modeled for the Chaser, including orbital disturbances and parametric uncertainties, related to the geometric and weight parameters.

The APF method has the task of attracting the chaser towards the target while ensuring collision avoidance of moving obstacles. They are considered to be spherical and with known radius. Moreover, the position of the obstacles is measured by LiDAR (Light Detection And Ranging) technology, with this sensor the obstacle is detected some meters before.

This scenario is simulated by Matlab software, in which the nonlinear dynamics and guidance and control algorithms are implemented. As briefly described above, the guidance function is based on the APF, while control laws are defined according to Sliding Mode Control, having regard to its features of both precision and robustness (insensibility to external disturbances). In particular a first-order Sliding Mode technique is used to ensure that the Chaser follows the chosen path, while a second-order SMC (Super-Twisting) makes sure that Chaser reaches the desired attitude.

This control strategy fits well with the actuation system of the Chaser. In fact, it consists of thrusters, that provide discontinuous forces with constant intensity (*on-off* functioning), and reaction wheels, used for a precise attitude control, by supplying a moment continuous in time, with a saturation value.

Thrusters dynamics and errors are taken into account. As regard the first aspect a low-pass filter is used to simulate a realistic behaviour of the thrust. Instead, both errors due to shooting direction and thrust magnitude are included. Including these errors implies that the thrusters produce a moment acting upon the spacecraft.

Extensive simulations guarantee the effectiveness of the proposed approach. Finally, the results show that the chaser is able to overcome obstacles and to approach the target.



# Sommario

Lo studio condotto nel presente progetto di tesi ha riguardato la manovra di *rendezvous*, in cui un satellite attivo (Chaser) deve avvicinarsi ad un satellite passivo (Target). In particolare, l'obiettivo di questo lavoro è stato quello di realizzare un algoritmo di guida e controllo capace di realizzare questa manovra in modo completamente autonomo.

Per prima cosa è stato condotto uno studio approfondito sull'argomento per capire vincoli e problematiche; fra di esse è emerso il pericolo di impatto con altri oggetti orbitanti, soprattutto i cosiddetti detriti spaziali (*space debris*). Queste potenziali collisioni sono pericolose per un duplice motivo: esse potrebbero danneggiare il satellite fino anche a causare la perdita della missione e la creazione di ulteriori detriti spaziali con una conseguente reazione a catena nota come Sindrome di Kessler.

Pertanto, al fine di realizzare una manovra di *rendezvous* in modo autonomo occorre uno strumento capace di rilevare eventuali ostacoli nello spazio intorno al Chaser, un sensore basato sulla tecnologia LiDAR (Light Detection And Ranging) viene proposto in questa tesi. Inoltre, l'algoritmo di guida che è stato sviluppato è basato sulla tecnica dei potenziali artificiali (*Artificial Potential Field, APF*). Questo metodo ha la fondamentale caratteristica di permettere una pianificazione del percorso *on-line* e quindi aggiornare la traiettoria calcolata verso il Target per tenere in considerazione i cambiamenti dell'ambiente circostante, come ad esempio il movimento di un ostacolo.

Per quanto riguarda il controllore, esso deve assicurare che il Chaser segua la traiettoria calcolata per mezzo dei potenziali artificiali e che il satellite si orienti come desiderato. La strategia di controllo proposta è quella dello Sliding Mode Control (SMC) viste le sue notevoli caratteristiche di precisione e robustezza (insensibilità ai disturbi esterni). In particolare si utilizza uno SMC del primo ordine per il controllo di posizione e uno del secondo ordine (Super-Twisting) per il controllo d'assetto. Queste strategie di controllo si adattano bene al sistema di attuazione del Chaser, che è composto da *thrusters* in grado di esercitare spinte discontinue e non modulabili (funzionamento *on-off*) e da ruote di reazione (*reaction wheels*) che applicano un momento che varia in modo continuo nel tempo e con un valore di saturazione. Un ulteriore vantaggio degli algoritmi proposti è il basso costo computazionale, che permette un'efficace implementazione *on-board*.

La combinazione APF/SMC è stata utilizzata per la prima volta da V.Utkin e J.Gulden nell'ambito della pianificazione del moto. L'innovazione proposta nel presente lavoro riguarda l'introduzione della dinamica dell'ostacolo nella pianificazione della traiettoria.

I risultati ottenuti mostrano come il Chaser sia in grado di avvicinare il Target rispettando i requisiti richiesti ed evitando gli ostacoli, ai quali è assegnata una geometria sferica di raggio noto, una posizione iniziale ed una velocità costante.

# Contents

<b>List of Figures</b>	IX
<b>List of Tables</b>	XI
<b>1 Introduction</b>	1
1.1 History of rendezvous maneuver . . . . .	1
1.2 The stages of the maneuver . . . . .	4
1.3 The space debris . . . . .	6
1.4 Overview of the work . . . . .	8
<b>2 Chaser configuration</b>	11
2.1 Models of sensors and actuators . . . . .	11
2.2 The attitude determination and control system . . . . .	13
<b>3 The orbital dynamic</b>	15
3.1 Reference frames . . . . .	15
3.1.1 Spacecraft local orbital frame $F_{l_o}$ . . . . .	15
3.1.2 Spacecraft attitude frame $F_a$ . . . . .	16
3.1.3 Coordinate transformation . . . . .	17
3.2 The equations of motion . . . . .	18
3.3 Trajectories for the closing phase . . . . .	19
3.3.1 Tangential boost transfer along V-bar . . . . .	20
3.3.2 Radial boost transfer along V-bar . . . . .	22
3.3.3 Straight line forced motion on V-bar . . . . .	23
3.3.4 Continuous thrust transfer along V-bar . . . . .	24
3.3.5 Choose of the trajectory type . . . . .	24
3.4 Cone of approach . . . . .	26
3.5 The attitude dynamic and kinematic . . . . .	27
<b>4 The guidance algorithms</b>	29
4.1 Path-planning among obstacles . . . . .	29
4.2 The construction of the artificial potential field . . . . .	31

<b>5</b>	<b>The control strategy</b>	37
5.1	First order Sliding Mode to position control . . . . .	38
5.2	Super-twisting Sliding Mode to attitude control . . . . .	39
<b>6</b>	<b>Simulations and results</b>	43
6.1	The simulation scenario . . . . .	43
6.2	The Matlab code . . . . .	45
6.2.1	The block of the Chaser dynamics . . . . .	46
6.2.2	The block of the Guidance law . . . . .	47
6.2.3	The block of the position control . . . . .	47
6.2.4	The block of the Attitude control . . . . .	48
6.2.5	Real effects . . . . .	48
6.3	Simulation results . . . . .	49
6.3.1	The radial boost with two obstacles . . . . .	50
6.3.2	The cone approach . . . . .	60
<b>7</b>	<b>Conclusions</b>	65
<b>8</b>	<b>Appendix</b>	67
8.1	Matlab script . . . . .	67
	<b>Bibliography</b>	81

# List of Figures

1.1	Gemini VII seen from Gemini VI . . . . .	2
1.2	Soyuz MS-07 and Progress MS-07 docked to ISS . . . . .	3
1.3	Phases of rendezvous and docking process [1] . . . . .	4
1.4	Definition of phase angle [2] . . . . .	5
1.5	The approach cone [3] . . . . .	6
1.6	Space debris in orbit around the Earth . . . . .	7
1.7	Evolution of the object in orbit around the Earth up to 2013 [5] . . . . .	8
2.1	Velodyne Lidar VLS-128 . . . . .	11
2.2	Thrust provided by the $i$ -th thruster switched on at time $t_0$ . [6] . . . . .	12
2.3	Thrust provided by the $i$ -th thruster switched on at time $t_0$ . [6] . . . . .	13
3.1	$F_{l_o}$ frame [2] . . . . .	16
3.2	$F_a$ frame [2] . . . . .	17
3.3	Euler angles . . . . .	18
3.4	Tangential impulse transfer along V-bar [2] . . . . .	20
3.5	Two-boost transfer maneuvers with finite pulse duration [2] . . . . .	21
3.6	Transfer along V-bar by radial impulses [2] . . . . .	22
3.7	Straight line V-bar trajectory [2] . . . . .	23
3.8	Transfer along V-bar by continuous z-thrust [2] . . . . .	25
3.9	Passively safe trajectories: radial boost transfer [2] . . . . .	25
3.10	Passively safe trajectories: tangential boost transfer [2] . . . . .	26
3.11	The cone of approach [7] . . . . .	26
3.12	Euler axis and Euler angle [8] . . . . .	28
4.1	Attractive and repulsive forces. [11] . . . . .	30
4.2	Parabolic potential field. [12] . . . . .	31
4.3	Relations among the vectors velocities. . . . .	33
4.4	Repulsive forces. . . . .	34
4.5	Total potential field. . . . .	35
5.1	The chattering phenomenon near a sliding surface [15] . . . . .	37
5.2	Feedback system . . . . .	38

5.3	Trajectory of the super-twisting controller [16] . . . . .	40
6.1	The two phases of the approach maneuver [6] . . . . .	43
6.2	Logical process of the Matlab code . . . . .	45
6.3	Matlab model for the simulation of the maneuvers . . . . .	46
6.4	Evolution of the trust over time . . . . .	49
6.5	Trajectory of chaser in the xz plane during the maneuver . . . . .	49
6.6	Trajectory of chaser in the xy plane during the maneuver . . . . .	50
6.7	Trajectory of chaser in the xz plane during the radial boost . . . . .	51
6.8	Trajectory of chaser in the xy plane during the radial boost . . . . .	51
6.9	Speed during radial boost . . . . .	52
6.10	Forces of the thrusters during radial boost . . . . .	53
6.11	Sliding surfaces of the guidance control during radial boost . . . . .	54
6.12	The Euler angles during radial boost . . . . .	55
6.13	The quaternions during radial boost . . . . .	56
6.14	Sliding surfaces of the attitude control during radial boost . . . . .	57
6.15	Torques provided by reaction wheels during radial boost . . . . .	58
6.16	Rotation speeds during radial boost . . . . .	59
6.17	Trajectory of the chaser in the xz plane during final approach . . . . .	60
6.18	Trajectory of the chaser in the xy plane during final approach . . . . .	61
6.19	Speed during final approach . . . . .	62
6.20	Forces during final approach . . . . .	63
6.21	Sliding surfaces of the guidance control during final approach . . . . .	64

# List of Tables

2.1	characteristics of the thruster. . . . .	13
6.1	Features of the chaser, of the initial orbit and of the obstacles. . . . .	44
6.2	The conditions of the chaser at the initial time of the two phases . . . . .	44



# Chapter 1

## Introduction

The effectiveness of the APF method is analyzed in this work as an instrument to achieve an autonomous rendezvous maneuver, in total safety and reliability.

One of the reasons why this study is carried out is the importance of the process of rendezvous in space missions. It consists of a series of orbital maneuvers with the aim of moving the satellite called chaser near a second spacecraft known as target.

The first successful rendezvous was in 1965 when the satellite Gemini VI was brought close to satellite Gemini VII through maneuvers performed by the human crew. In 1967 instead, the Soviets realized the first automatic rendezvous, the latter process brings about noticeable benefits, although it is complicated to implement.

The present work fits into this context, with the aim of achieving a collision-free path for the chaser towards the target. With respect to the impacts, the greatest danger is from space debris, namely vehicles, or part of them, abandoned by the man at the end of their operational life. It is essential that the satellite can detect and work around these obstacles because an impact could lead to the loss of the mission.

In addition, each impact creates new debris, so the density of objects in orbit around the Earth increases, this leads to an increased risk of new impacts. This is the scenario proposed by Kessler in 1978 and called Kessler syndrome. Its direct consequence is that the increasing number of debris in orbit would make impossible the use of artificial satellites. For the reasons mentioned above the issue of obstacle avoidance takes on considerable importance in space missions.

### 1.1 History of rendezvous maneuver

On 15 December 1956 the Gemini 6 and Gemini 7 mission made history by performing for the first time a piloted rendezvous between two manned spacecraft. However, this was not the original NASA's idea, because Gemini VI was supposed to rendezvous and docking with an appropriate satellite: the GATV-6, but it exploded during launch, so a



**Figure 1.1:** Gemini VII seen from Gemini VI

second Gemini capsule took the place of the previous vehicle.

Gemini VII was launched into orbit on 5 December, the launch of Gemini VI took place on 15 December after two failed attempts, and it met the Gemini VII capsule during the fourth orbit around the Earth.

Walter Schirra, commander, and Thomas Stafford as the pilot composed the crew of Gemini VI. They managed to take at a minimum distance of 30 cm from Gemini VII during subsequent rendezvous maneuvers. Astronauts Borman and Lovell were the crew of Gemini VII. They were pretty passive during approaching maneuvers as the capsule was in space for several days and had to save fuel. Figure 1.1 shows a vision of the spacecraft Gemini VII from Gemini VI.

This mission demonstrated the high accuracy with which could be piloted Gemini capsules. However, it was not possible to carry out the engagement, as there was not the necessary mechanism in Gemini VII.

The next mission Gemini had the objective to compensate for this lack, and in March of 1966, Gemini VIII capsule docked successfully to an Agena Target Vehicle. The latter was designed to allow the rendezvous maneuver and docking of two spacecraft in orbit.

On 30 October 1967, the Soviets performed for the first time a fully automatically rendezvous maneuver and docking. For this mission two spacecraft Soyuz-type were employed: Cosmos 186 was the active satellite, equipped with the docking system, while



**Figure 1.2:** Soyuz MS-07 and Progress MS-07 docked to ISS

Cosmos 188 was the passive one.

The maneuver was not perfect for a variety of reasons. Cosmos-186 missed the other satellite of about 900 meters during the first attempt. On the second try, the docking took place from a mechanical point of view, but not from the point of view of electronic systems. This due to a small lateral motion of the spacecraft during the last phase of approach.

However, the main problem was that the fuel consumption was significantly higher than calculated. To perform the maneuver, Cosmos-186 had to ignite the thrusters 28 times, pushing for a total of 200 seconds.

In any case, the mission showed that a fully automatic rendezvous maneuver and docking between two spacecraft was achievable. This opened the way to the possibility of carrying in orbit a large load by breaking it down into small pieces to assemble them directly in space. This solution offers smaller rockets and thus it allows to save money. Automated rendezvous and docking also had a fundamental importance in the Apollo program of Americans and the future construction of space stations.

In fact, a rendezvous takes place each time a spacecraft brings supplies or crew members to an orbiting space station. This happened for the first time in 1971 when the satellite Soyuz 11 carried three cosmonauts to the space station Salyut 1. Subsequently, rendezvous missions were conducted to reach various space stations, such as Skylab, Mir, and the International Space Station (ISS). Currently, Soyuz spacecraft are used to transfer the crew members to and from ISS, while Progress spacecraft is used to resupply the station and to reboost it into a higher orbit while docked. In the past also the Europe's Automated Transfer Vehicle did these tasks, but the program closed in 2015.

Rendezvous missions were also conducted to expand the space stations directly into orbit. This happened for the first time in 1987 when the module Kvant 1 docked to Mir

space station, and then the procedure was used to assemble the ISS.

Two onboard systems play a key role in the success of an automatic rendezvous and docking maneuver: the Guidance, Navigation and Control (GNC) system determines and controls the position of the center of mass of the satellite, while the Attitude, Determination and Control System (ADCS) determines and controls the orientation of the same relative to its center of mass.

## 1.2 The stages of the maneuver

A rendezvous and docking process can be divided into different phases such as:

- Launch and orbit injection,
- Phasing and transfer to near target orbit,
- Far range rendezvous operations,
- Close range rendezvous operations,
- Final approach to contact.

They are showed schematically in chronological order in Figure 1.3.

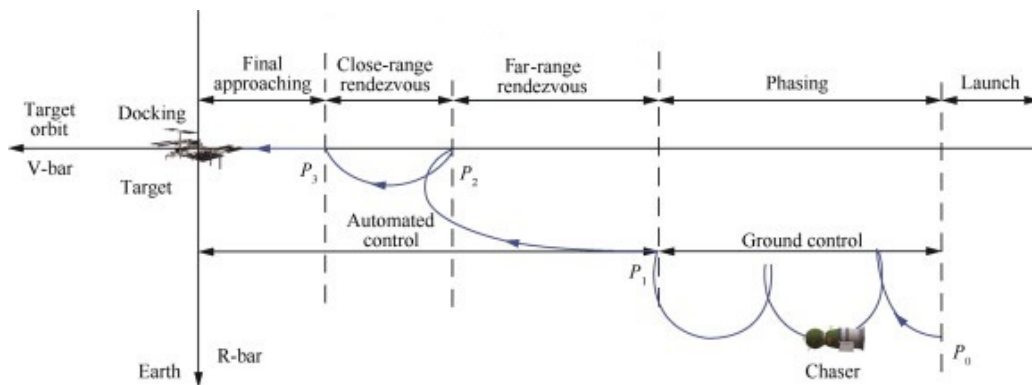


**Figure 1.3:** Phases of rendezvous and docking process [1]

The aim of the launch is to put the chaser into an orbit in the same orbital plane of the target. Therefore, the launch window must be chosen based on the capacity to correct the orbital plane of the launcher. At the end of the launch phase, the chaser is on the same orbital plane of the target, it's on a lower orbit and may be at an arbitrary phase angle behind the target. (Figure 1.4)

During the phasing the chaser is controlled by ground stations, the purpose is to bring the satellite within the communication area of the target so that the relative navigation can

begin. At this stage phase angle between chaser and target is reduced, exploiting their different orbital height, and the orbit of the chaser is raised. In addition, at this stage a drift motion occurs because of the time that the relative navigation sensors employ to converge, and to prepare the next transfer maneuver. The end point of this stage is called ‘initial aim point’ ( $P_1$  in Figure 1.3). Its location depends on several factors, the most important of them are the location of the docking port, the direction of the docking axis and the operational range of the navigation sensor.

The main purposes of the far range rendezvous operations phase, also called ‘homing’, are to reach the target orbit and to reduce the relative velocity of the chaser. From this stage forward navigation is based on measurements of relative position to the target, then homing can start when relative navigation between chaser and target is available. The position of the endpoint of this phase can be affected by requirements dictated by the target. For the ISS, for example, the point  $P_2$  in Figure 1.3 must be outside the Approach Ellipsoid, which has a major half-axis of 2 km and minor ones of 1 km.

A ‘hold point’ may be used at the end of the far range rendezvous phase, in order to synchronize the mission timeline with external events, such as Sun illumination, communication windows and crew operations timeline. This is a point where the chaser can stay indefinitely at nominally zero  $\Delta V$  costs.

The objective of the close range rendezvous operations, also called ‘closing’ phase, is to reduce to few hundred meters distance from the target, while the starting value is some units of km. At the end of this phase the chaser has reached the position, velocity, attitude and angular rates conditions to approach the final corridor. Different type of maneuvers can be chosen for the approach. In this thesis, a radial boost maneuver is analyzed, because of its inherent collision safety. At this point the final approach begins. The goal is to reach the position, velocity, attitude and angular rates conditions whereby the docking

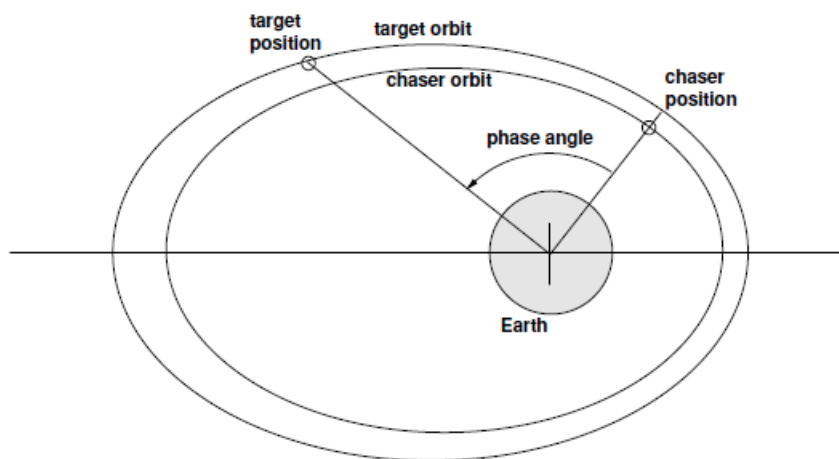


**Figure 1.4:** Definition of phase angle [2]

can be carried out. At this stage the chaser follows a straight line trajectory or quasi-straight line trajectory; in any case the satellite must remain within a cone of approach that is defined for safety reasons. The cone originates from the mating point at the target vehicle, i.e. from the docking port, and has a half cone angle of 10–15 deg. If the satellite exceeds the limits of the cone, a stop or a collision avoidance maneuver must be made. The chaser must follow the docking axis, and this is only possible if the rendezvous sensors for the final approach are able to measure, in addition to axial and lateral positions, the relative attitude between the docking ports of chaser and target. Once the capture interface of chaser arrives within the reception range, the docking mechanism must make the capture. [2]

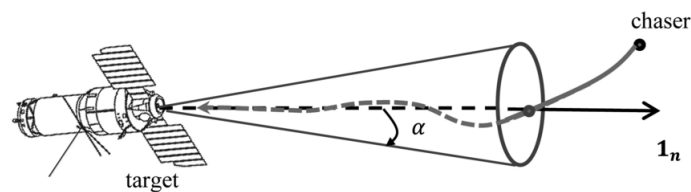


Figure 1.5: The approach cone [3]

### 1.3 The space debris

The topic of space debris plays a very important role in this thesis. In fact, to ensure that the maneuver will be done successfully is not enough to carry out it as described in Section 1.2. It is also necessary that the chaser can detect the presence of physical constraints along its trajectory and, by means of guidance and control laws, ensure their avoidance. These obstacles can be still active satellites, micrometeoroid, or, more likely, space debris. They are vehicles, or part of them, abandoned by the man at the end of their operational life and still in orbit around the Earth.

A collision is dangerous not only in terms of the loss of the mission, but each impact into orbit creates more space debris, this chain reaction can in the long term lead to entrapment in our planet, i.e. the impossibility to carry out space missions. This scenario was proposed to NASA by the astrophysicist Donald J. Kessler in 1978, and is called Kessler syndrome.

From the beginning of space operations, about 60 years ago, the number of objects in orbit around the Earth vertiginously increased, as the Figure 1.7 shows. Approximately 8 000 satellites were launched, and most of them ended their operational lives, becoming space debris. Some of them are fragmented, creating additional smaller debris. In addition, it should be added to the count the rocket stages.

In order to mitigate this problem, NASA has stipulated regulations. One example is the upper stage passivation of launch vehicles, to reduce the risk of explosion in orbit.



**Figure 1.6:** Space debris in orbit around the Earth

Another example is the direct deorbit at the end of the operating life, or a maneuver that accelerates the deorbit by means of atmospheric drag if the first option is too expensive. At orbital altitudes where the previous maneuvers are not feasible, the old satellites must be placed on a ‘graveyard orbit’, that does not intersect with other commercial or scientific orbits.

Within this scenario, another important issue is the collision avoidance. In fact, a well known example of the seriousness of the impacts between satellites occurred in 2008, when inactive satellite Cosmos 2251 hit the active satellite Iridium 33. This provoked the biggest increase of the space debris.

At present over 25 000 orbiting objects larger than 10 cm are monitored, but a much larger number has a smaller size and cannot be traced. These objects can reach speeds of the order of 25 000 Km/h, then an impact could cause serious damage despite their small size. The greatest danger relates to the ISS and manned spacecraft. They are typically equipped with shields to dampen the impact damage, but beyond this precaution, NASA has guidelines to avoid this danger. They are based on the probability of collision between the satellite and debris: when this probability reaches the limit values an evasive maneuver must be accomplished.

To calculate the probability of collision, NASA uses two formulas: if the orbital debris flux is known, the equation 1.1 provides the needed information. Instead the equation 1.2 is used if the spatial density is known.

$$F_d \cdot A_t \cdot t \quad (1.1)$$

$$v_m \cdot A_t \cdot \rho_s \cdot t \quad (1.2)$$

$F_d$  is the orbital debris flux,  $A_t$  is the cross-sectional area,  $t$  is the time,  $v_m$  is the average collision velocity and  $\rho_s$  is the spatial density.

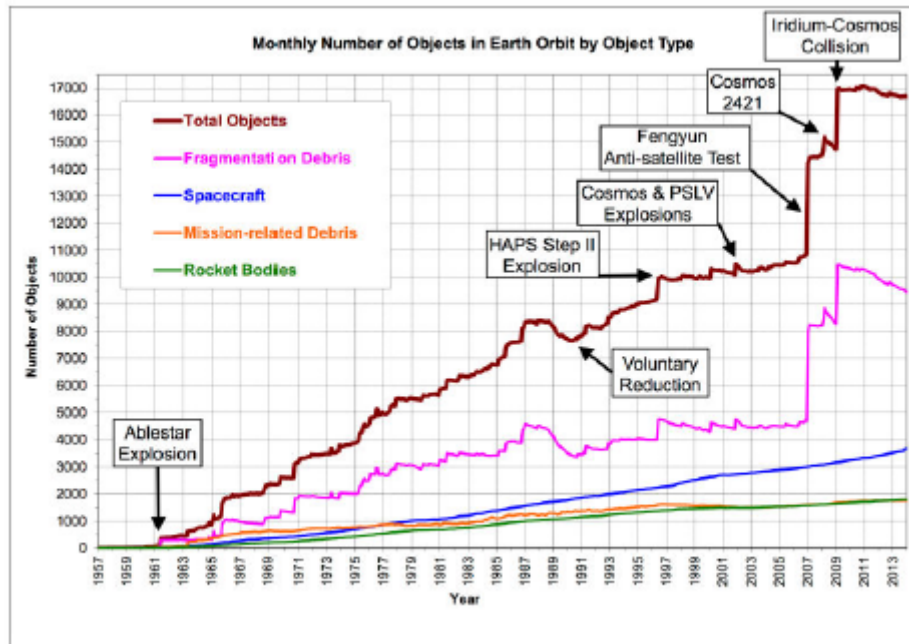


Figure 1.7: Evolution of the object in orbit around the Earth up to 2013 [5]

NASA guidelines dictate that if the probability of collision with a manned satellite is greater than 1 in 10 000, a collision-avoidance maneuver must be performed; instead, if the probability is greater than 1 in 100 000, a collision-avoidance maneuver is performed if it does not compromise the mission objectives. No maneuver is needed if the probability is smaller than 1 in 100 000. [4]

In the case of the space station, sometimes there is no time to change the orbit. If this happens, the astronauts have to come aboard Soyuz capsules. These would be used as lifeboats in case of an impact capable to compromise the survival of the station.

## 1.4 Overview of the work

To achieve the purpose of this thesis, first of all it was performed a research on the rendezvous maneuver. This in order to understand its complexity, the trajectories that should be followed and safety constraints to the successful conclusion of the operation. Then it was conducted a study on the dynamics governing the issue, that is based on the equations of relative motion of Hill-Clohessy-Wiltshire. Subsequently, it was taken into account several strategies to guide and control before choosing the combination given by Artificial Potential Field and Sliding Mode Control (SMC). V.I.Utkin and J.Gulden were among the first users of this strategy. The APF is tasked to find in real-time the path that

the chaser must follow towards the target. It consists of a portion that provides the attractive force toward the goal position, and another one that provides the repulsive effect around the obstacles. SMC instead is responsible for ensuring that the chaser follows the path set by the APF. This is an effective and adequate control strategy to be implemented through mono-directional actuators. Matlab software is used to implement the nonlinear dynamic orbital and a guide and control algorithm.

The body of the thesis is divided into 5 chapters as follows.

Chapter 2 introduces the configuration of the chaser, focusing on GNC system and ADCS. Chapter 3 provides a description of the reference frames used in orbit and the transformation between them. Also, it elaborates on the Chaser dynamics and the trajectories, followed during approach.

Chapter 4 shows the various techniques used in automation for motion planning. Then, it delves into the artificial potential field method, and it provides the equations used in this thesis to lead the satellite toward the target, avoiding obstacles at the same time.

Chapter 5 provides first a description about the methodology of the Sliding Mode Control (SMC), focusing on both its advantages and its weakness. Then the equations of both the first-order SMC to navigation control and the Super-Twisting SMC to attitude control are reported.

Finally, Chapter 6 describes the simulation scenario and the Matlab code, which incorporates non-linear orbital dynamics within the algorithm of guidance and control. Then it discusses the results obtained.



# Chapter 2

## Chaser configuration

### 2.1 Models of sensors and actuators

In satellites, GNC system has the task to determine and to track the desired trajectory. The study of this thesis begins in the ‘Closing’ phase, when the motion of the Chaser is studied relative to the Target. The relative navigation is based on the ‘Relative GPS’ (RGPS) principle. In this principle, measurement of both relative range and range-rate are calculated by the subtraction of the state vector, measured with GPS, of both target and chaser. [2] So, to accomplish this type of navigation, GPS receivers have to be installed on the spacecraft.

Instead, to detection obstacles, the Velodyne Lidar VLS-128 is used (Figure 2.1), which has a range of 300 *m* and weighs 3.53 *kg*. It exploits the Light Detection And Ranging technology (LiDAR), which makes it possible to determine the distance of an object by using a laser pulse.



**Figure 2.1:** Velodyne Lidar VLS-128

This sensor can also be used to drive the chaser to the target during the last phase of the maneuver, i.e. in the approach cone.

The actuation system of the chaser exploits thrusters to position control. They can exert mono-directional thrust of given magnitude and along fixed directions; In addition, the figure 2.2 shows that they have only two modes of operation:

- On, the thruster provide the maximum value of thrust,
- Off, the thrust is zero.

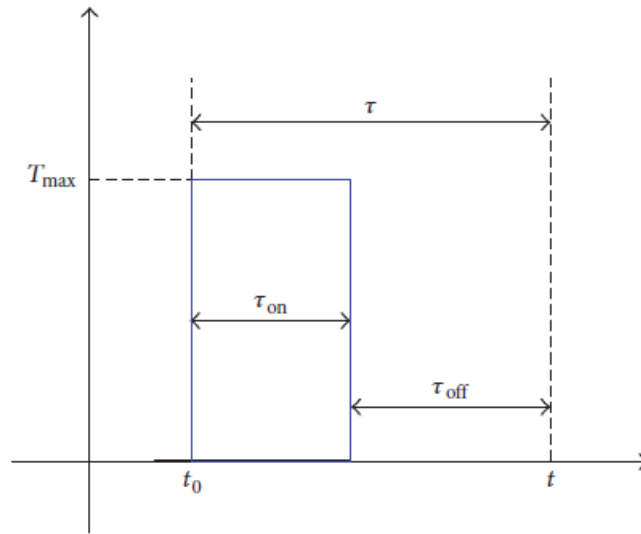


**Figure 2.2:** Thrust provided by the  $i$ -th thruster switched on at time  $t_0$ . [6]

So, the thruster behavior can be resumed in Equation 2.1:

$$T = \begin{cases} T_{max}, & \text{if } t \in (t_0, t_0 + \tau_{on}) \\ 0, & \text{if } t \in (t_0 + \tau_{on}, t_0 + \tau_{on} + \tau_{off}) \end{cases} \quad (2.1)$$

$\tau_{off}$  indicates the time in which the thruster must stay off after that it switched to  $T = 0$ . This value is related to the frequency of thruster.

On spacecraft, two actuators are installed in each direction in which the control is required, as Figure 2.3 shows, and they are always switched on at the same time. In this way the system delivers a zero nominal torque, not including errors of thrust and of installation.

In this work, a thruster Globalstar Cosmo-Skymed 2 Herschel Planck was chosen to equip the chaser. Its characteristics are shown in Table 2.1.

Parameter	Value	Unit of measure
Thrust nominal	1	$N$
Specific Impulse nominal	220	$s$
Mass thruster with valve	290	$g$
Frequency <sup>1</sup>	50	$Hz$

**Table 2.1:** characteristics of the thruster.

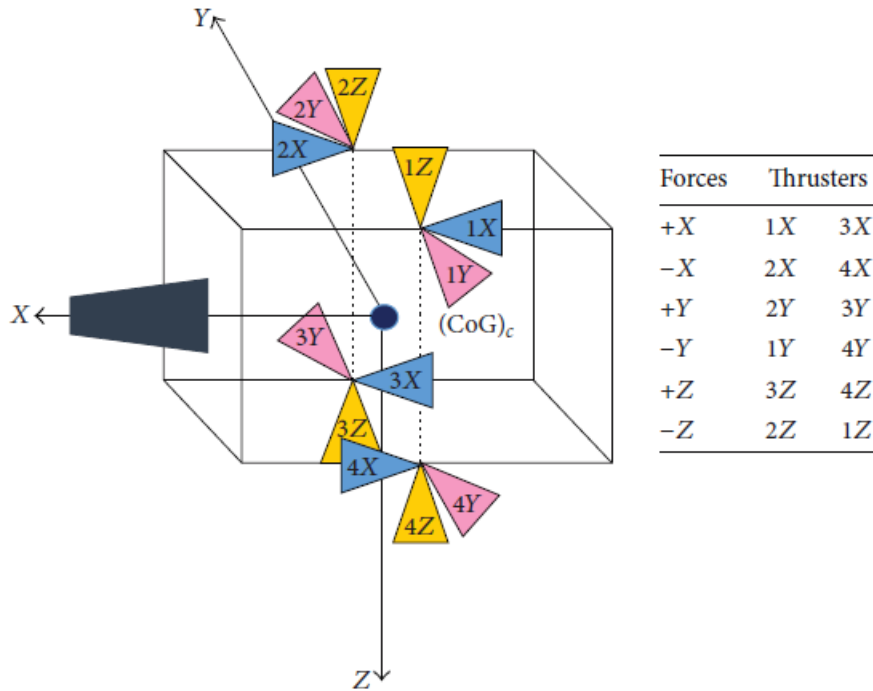


**Figure 2.3:** Thrust provided by the  $i$ -th thruster switched on at time  $t_0$ . [6]

## 2.2 The attitude determination and control system

This system of the spacecraft is also known under its abbreviation ‘ADCS’. It is responsible both for determining the current orientation and for controlling to rotate the satellite in the desired attitude. The satellite may need to be oriented to the payload requirements; However this is not considered in this thesis and the desired attitude is determined from the maneuver to be carried out.

Two star-tracker, assembled so that their axes are perpendicular, and an Inertial Measurement Unit (IMU) is a common configuration to provide measurement of attitude and angular-rate of a spacecraft. So it is the one used on the chaser during the radial boost,

while in the cone of approach both relative orientation and relative angular-rate to the target can be provided by LiDAR.

Instead, the reaction wheels provides attitude control. The minimum configuration is to install a wheel for each of the three body axes, but to ensure redundancy in case of failure it takes four wheels in a tetrahedral configuration.

Putting into rotation the wheel, the satellite rotates in the opposite direction in order to maintain a constant angular momentum of the system. Also, reaction wheels are able to counter the external torques: they tend to change the angular momentum of the satellite  $\vec{H}_{S/C}$ , then the wheel is spun at higher speeds, so its angular momentum  $\vec{H}_{wheel}$  increases and  $\vec{H}_{S/C}$  decreases, according to the conservation of total momentum. (Equation 2.2)

$$\vec{H} = \vec{H}_{S/C} + \vec{H}_{wheel} \quad (2.2)$$

As a result, the rotation speed corresponding to the zero rotation of the satellite increase; When the angular velocity exceeding structural limits, wheels must be desaturated, i.e. they are stopped and the  $\Delta \vec{H}$  that the satellite tends to regain is canceled by a secondary propulsion system.

To avoid transients and friction to change of sign of the angular velocity, the wheels are pre-loaded at low rpm. The disadvantage is the need to desaturate most often. [5]

# Chapter 3

## The orbital dynamic

This chapter provides first a description of the reference frames used in space flight and how to do a change of coordinates between them; then the equations of relative motion are presented and several kinds of approaching maneuvers are described. Finally it explains how to calculate and represent the attitude of the satellite.

### 3.1 Reference frames

A coordinate frame  $F_i$  is defined by its origin  $O_i$  and from a set of three orthogonal unit vectors  $\vec{a}_1, \vec{a}_2, \vec{a}_3$ . To describe the motion of a satellite typically need three different systems:

- *Orbit reference frame*, to describe the orbit covered by satellite and the motion of the same within the orbit, relative to inertial space and to the Earth;
- *Spacecraft local orbital reference frame*, to describe the motion relative to a particular point in orbit or to another spacecraft;
- *Spacecraft attitude and body frame*, to describe the attitude dynamic and kinematic of the spacecraft, relative to its center of mass. Furthermore this system is useful to represent the characteristics relating to the geometry of the spacecraft.

The study of this thesis starts when relative navigation is already achieved, then the first of the three types of reference frames is not in the interest of this work. Below the frames used are described; then it is shown how to make a change of coordinates between them.

#### 3.1.1 Spacecraft local orbital frame $F_{1o}$

This frame is used to describe the motion of the chaser w.r.t. the target; both are shown as points, and not as 3D objects, as they are actually. This is the coordinate frame necessary

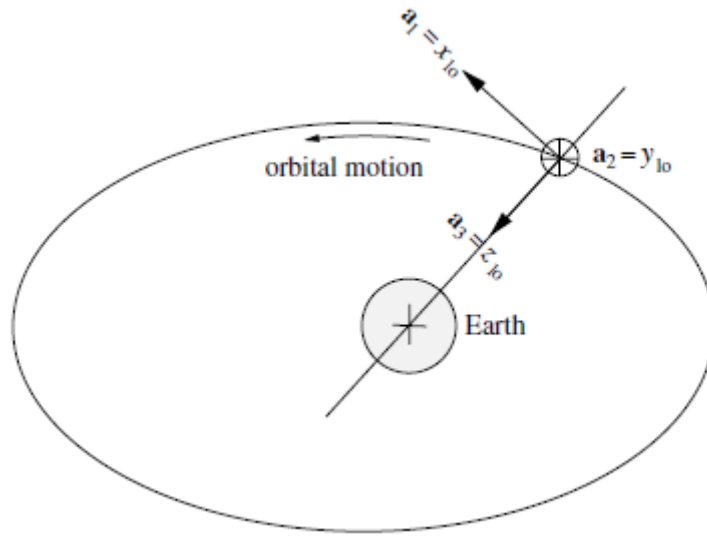


**Figure 3.1:**  $F_{l_o}$  frame [2]

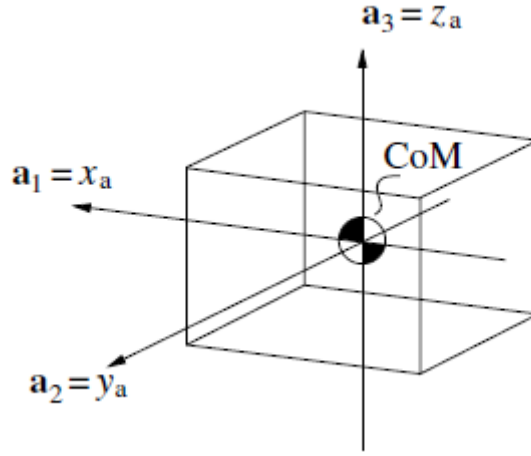
to perform the navigation function: the approach trajectory of the chaser is shown in this frame, which is often referred to as the local-vertical/local-horizontal (LVLH) frame. It is explained in Figure 3.1, where:

- $O_{l_o}$  is the origin of the frame, it is the center of mass of the target;
- $\vec{a}_1$  is the unit vector in the direction of the orbital speed, but it is not necessarily aligned with it since it is taken as  $\vec{a}_1 = \vec{a}_2 \times \vec{a}_3$ . The axis identified by this unit vector is also called ‘V-bar’ in the rendezvous literature;
- $\vec{a}_2$  is the unit vector pointing in the opposite direction to the angular momentum vector of the orbit. In rendezvous, this coordinate is also called ‘H-bar’;
- $\vec{a}_3$  is the unit vector pointing towards the centre of the Earth. The axis identified by  $\vec{a}_3$  is also called ‘R-bar’ in rendezvous.

### 3.1.2 Spacecraft attitude frame $F_a$

This frame is also called ‘body frame’; however, it is not fixed due to the geometry of the spacecraft. In fact the center of mass moves during the flight because of fuel consumption. The attitude frame is used to describe the rotations made by the spacecraft, which is then seen as a 3D object.  $F_a$  is employed in the ADCS, and it is shown in Figure 3.2.

- $CoM$  is the origin of the frame, it is the center of mass of the target;
- $\vec{a}_1$ , in the final phase of a rendezvous and docking mission this unit vector is collinear to the docking axis, which is directed along V-bar in this work;


 Figure 3.2:  $F_a$  frame [2]

- $\vec{a}_2$  is often aligned with the positive or negative direction of the angular momentum vector of the orbit;
- $\vec{a}_3$  is determined by the right hand rule:  $\vec{a}_3 = \vec{a}_1 \times \vec{a}_2$ .

### 3.1.3 Coordinate transformation

In sections 3.1.1 and 3.1.2 were defined the reference frames. It is possible to make a change of coordinates, for example, to switch from the body frame to the LVLH frame. This can be done with a rotation of the frame, which is defined analytically from the rotation matrix, built with the Euler angles  $\phi, \theta, \psi$ . This allows to match the dynamics of position with the attitude dynamic.

Figure 3.3 provides the relation between the rotation of the coordinate frame and the Euler angles. In the case shown, to switch from frame  $F_a$  to system  $F_{lo}$ , a rotation  $123$  is used; so as a first step the system  $F_a$  is rotated around the axis  $x_a$  of an amount equal to the angle  $\phi$ . Later the frame is rotated around the axis  $y'_a$  of an amount equal to the angle  $\theta$ ; finally, with a rotation  $\psi$  around axis  $z''_a$ , the system  $F_{lo}$  is obtained.

So the process consists of three basic rotations, each of which can be described by a rotation matrix. The product of these returns the complete rotation matrix. (Equation 3.1) Then the desired coordinate change is calculated as shown in Equation 3.2.

$$\begin{aligned}
 A_{123}(\phi, \theta, \psi) &= A_3(\psi) \cdot A_2(\theta) \cdot A_1(\phi) = \\
 &= \begin{bmatrix} \cos \psi & -\sin \psi & 0 \\ \sin \psi & \cos \psi & 0 \\ 0 & 0 & 1 \end{bmatrix} \cdot \begin{bmatrix} \cos \theta & 0 & \sin \theta \\ 0 & 1 & 0 \\ -\sin \theta & 0 & \cos \theta \end{bmatrix} \cdot \begin{bmatrix} 1 & 0 & 0 \\ 0 & \cos \phi & -\sin \phi \\ 0 & \sin \phi & \cos \phi \end{bmatrix} \quad (3.1)
 \end{aligned}$$

$$\begin{bmatrix} x_{lo} \\ y_{lo} \\ z_{lo} \end{bmatrix} = A_{123}(\phi, \theta, \psi) \cdot \begin{bmatrix} x_a \\ y_a \\ z_a \end{bmatrix} \quad (3.2)$$

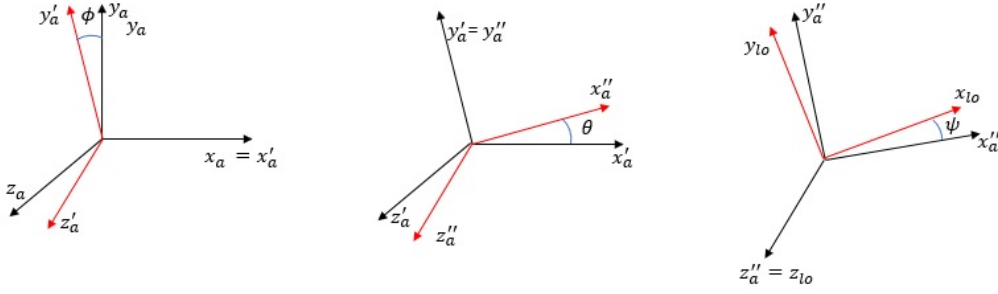


Figure 3.3: Euler angles

## 3.2 The equations of motion

As mentioned in the subsection 3.1.1, in rendezvous trajectories it is convenient to adopt the  $F_a$  reference frame, centered in the center of mass of the target. The motion of the chaser in this frame is described by the Hill equations of relative motion; which are valid in the  $F_a$  system in the case of circular orbits. (Equation 3.3)

$$\begin{cases} \ddot{x} - 2\omega\dot{z} = \frac{1}{m_c} F_x \\ \ddot{y} + \omega^2 y = \frac{1}{m_c} F_y \\ \ddot{z} + 2\omega\dot{x} - 3\omega^2 z = \frac{1}{m_c} F_z \end{cases} \quad (3.3)$$

The parameters that appear in the Equation 3.3 are explained below.

$x$  is the coordinate along ‘V-bar’,  $y$  is related to ‘H-bar’ and  $z$  is ‘R-bar’. Together, they form the position vector of the chaser.  $\omega = \frac{\mu}{r_t}$  is angular velocity with which the target, i.e. the origin of the frame LVLH, rotates around the center of mass of the Earth, from which it is distant  $r_t$ .  $m_c$  is the mass of the chaser, which varies over time due to the action of thrusters. Finally,  $F_x, F_y, F_z$  are the forces applied to the chaser. They are the three components of the force vector  $\vec{F}$ ; which is the sum of two contributions of different nature, as Equation 3.4 shows.

$$\vec{F} = \vec{F}_{thr} + \vec{F}_{ex} \quad (3.4)$$

$\vec{F}_{thr}$  is the vector of the forces provided by the actuators described in section 2.1; while  $\vec{F}_{ex}$  is the the vector of external forces, produced by atmospheric residue, by the effect of

crushing of the Earth at the poles, and by the solar radiation pressure.

The orientation of the thrusters is known relative to the body frame, so  $\vec{F}_{thr}$  is defined in  $F_a$  ( $\vec{F}_{thr} = \vec{F}_{thr}(\vec{x}_a)$ ); However, it is necessary to know the vector of forces in the LVLH frame, in order to insert it into the system 3.3. Then  $\vec{F}$  must be rotated, applying the rotation matrix in Section 3.1.3. This matches the attitude dynamic to position dynamic, because from the first the Euler angles are taken; then they are used to derive the component of the force to be included in the equations of motion.

$$\vec{F}_{thr}(\vec{x}_{lo}) = A_{313}(\phi, \theta, \psi) \cdot \vec{F}_{thr}(\vec{x}_a) \quad (3.5)$$

W. H. Clohessy and R. S. Wiltshire derived a linearised solution of the Hill equations, which is valid for distances between chaser and target that are very small compared with the distance to the centre of the Earth. This solution is shown in Equations 3.6; where  $\gamma$  is the constant acceleration and the subscript ‘0’ indicates the initial conditions.

$$\left\{ \begin{array}{l} x(t) = \left( \frac{4\dot{x}_0}{\omega} - 6z_0 \right) \sin(\omega t) - \frac{2\dot{z}_0}{\omega} \cos(\omega t) + (6\omega z_0 - 3\dot{x}_0)t + \left( x_0 + \frac{2\dot{z}_0}{\omega} \right) + \\ \quad + \frac{2}{\omega^2} \gamma_z (\omega t - \sin(\omega t)) + \gamma_x \left( \frac{2}{\omega^2} (1 - \cos(\omega t)) - \frac{3}{2}t^2 \right) \\ y(t) = y_0 \cos(\omega t) + \frac{\dot{y}_0}{\omega} \sin(\omega t) + \frac{\gamma_y}{\omega^2} (1 - \cos(\omega t)) \\ z(t) = \left( \frac{2\dot{x}_0}{\omega} - 3z_0 \right) \cos(\omega t) + \frac{\dot{z}_0}{\omega} \sin(\omega t) + \left( 4z_0 - \frac{2\dot{x}_0}{\omega} \right) + \\ \quad + \frac{2}{\omega^2} \gamma_x (\sin(\omega t) - \omega t) + \frac{\gamma_z}{\omega^2} (1 - \cos(\omega t)) \end{array} \right. \quad (3.6)$$

### 3.3 Trajectories for the closing phase

As mentioned in Section 1.2, both the starting point and the end point of the closing phase are on the same orbit of the target; the goal is to reduce the distance between it and the chaser to few hundred meters.

The trajectory of this stage can be chosen between four different types:

- tangential boost transfer along V-bar;
- radial boost transfer along V-bar;
- straight line forced motion on V-bar;
- continuous thrust transfer along V-bar.

Below, they are analyzed in the nominal case (i.e. ideal trajectories); then the reasons that lead to the choice of the type of maneuver are shown.

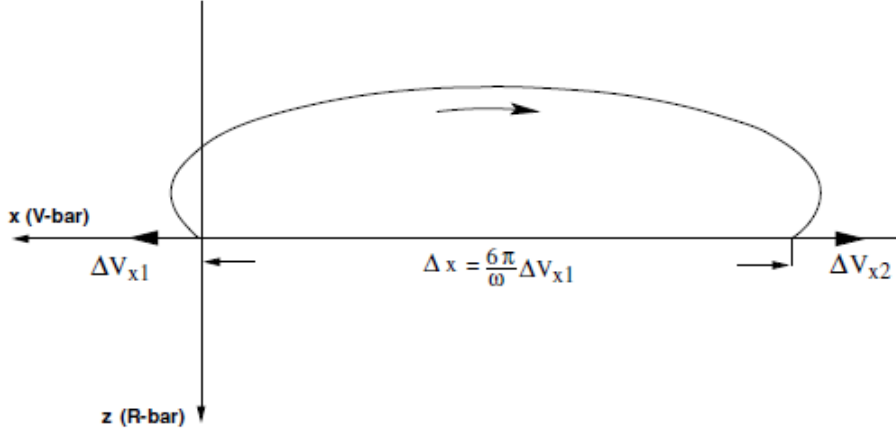


Figure 3.4: Tangential impulse transfer along V-bar [2]

### 3.3.1 Tangential boost transfer along V-bar

In a first approximation, it may be treated as a maneuver that uses two impulses of velocity in the x-direction, i.e. an instantaneous change of velocity at the time of the maneuver. Actually, there are no purely impulsive maneuvers; but this is a good approximation to derive the  $\Delta V$  need to get a certain trajectory.

Since the change of velocity is instantaneous, accelerations  $\gamma$  are zero, while the following initial conditions are taken:

$$x_0 = y_0 = z_0 = 0 \quad \dot{x}_0 = \Delta V_x \quad \dot{y}_0 = \dot{z}_0 = 0$$

Inserting these conditions in Equation 3.6, they become:

$$\begin{cases} x(t) = \frac{1}{\omega} \Delta V_x (4 \sin(\omega t) - 3\omega t) \\ y(t) = 0 \\ z(t) = \frac{2}{\omega} \Delta V_x (\cos(\omega t) - 1) \end{cases} \quad (3.7)$$

The goal of this maneuver is solely a change of position along V-bar, i.e. it is  $\Delta x = x_f - x_0$ . Therefore the duration of the maneuver is  $t = T$ , with  $T$  orbital period; so  $\omega t = 2\pi$  and from Equation 3.7 is obtained that:

$$\begin{cases} x_f = -\frac{6\pi}{\omega} \Delta V_{x1} \\ y_f = 0 \\ z_f = 0 \end{cases} \quad (3.8)$$

Then the first impulse is set based on the  $\Delta x$  to be achieved:  $\Delta V_{x1} = -\frac{\omega}{6\pi} \Delta x$ . The second impulse is equal to the first, then the total change of velocity required is:  $\Delta V =$

$|\Delta V_{x1}| + |\Delta V_{x2}| = \frac{\omega}{3\pi} \Delta x$ . Figure 3.4 provides the trajectory resulting from this maneuver.

As mentioned previously in this section, there are no purely impulsive maneuvers. In reality all propulsive systems have a finite force level, so it has to be applied over a certain time in order to achieve the desired  $\Delta V$ . Given the acceleration  $\gamma_x$ , this time can be determined as  $\tau = \frac{\Delta V}{\gamma_x}$ ; while the initial conditions become:

$$x_0 = y_0 = z_0 = 0 \quad \dot{x}_0 = \dot{y}_0 = \dot{z}_0 = 0 \quad \gamma_y = \gamma_z = 0$$

Inserting them in the Equations 3.6 the equations of motion during the boost are obtained:

$$\begin{cases} x(t) = \frac{1}{\omega^2} \gamma_x (4(1 - \cos(\omega t)) - \frac{3}{2} \omega^2 t^2) \\ y(t) = 0 \\ z(t) = \frac{2}{\omega^2} \gamma_x (\sin(\omega t) - \omega t) \end{cases} \quad (3.9)$$

The velocities during the boost are obtained by deriving the Equations 3.9:

$$\begin{cases} \dot{x}(t) = \gamma_x \left( \frac{4}{\omega} \sin(\omega t) - 3t \right) \\ \dot{y}(t) = 0 \\ \dot{z}(t) = \frac{2}{\omega} \gamma_x (\cos(\omega t) - 1) \end{cases} \quad (3.10)$$

Between a boost and the other, there is the phase of free-drift, in which Equations 3.7 are those of reference. The duration of this phase is still an orbital revolution, so the distribution of the time of the maneuver is the one in the Figure 3.5.

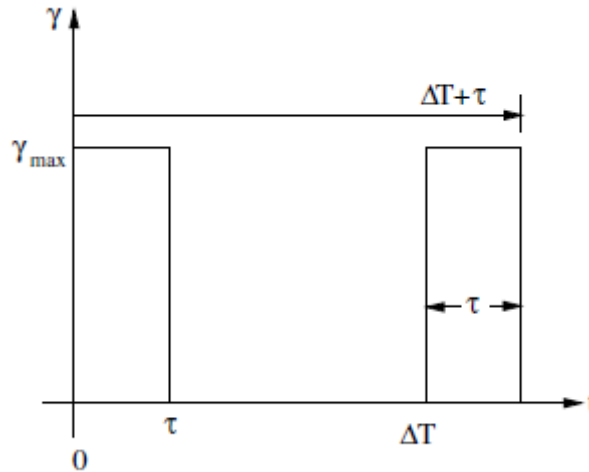


**Figure 3.5:** Two-boost transfer maneuvers with finite pulse duration [2]

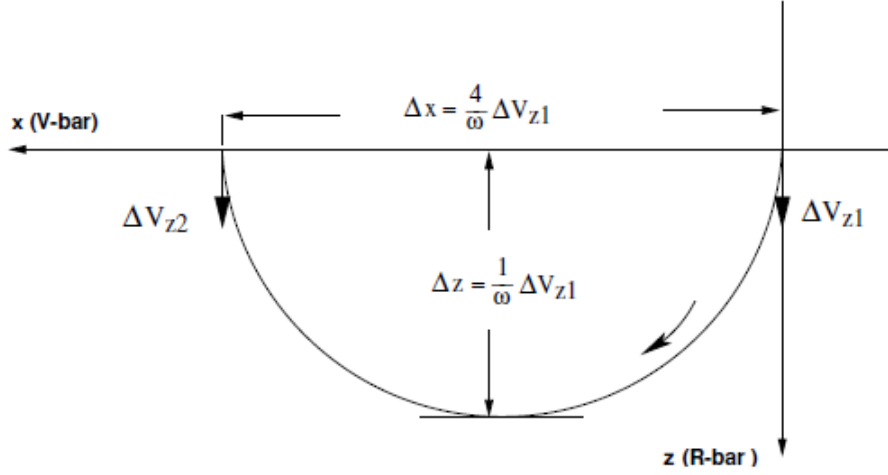


Figure 3.6: Transfer along V-bar by radial impulses [2]

### 3.3.2 Radial boost transfer along V-bar

This maneuver is similar to the one described in Subsection 3.3.1: the goal is the same and it consists of two impulses of velocity, but in the  $z$ -direction instead of  $x$ .

In the approximation of purely impulsive maneuver, the initial conditions are the following:

$$x_0 = y_0 = z_0 = 0 \quad \dot{x}_0 = \dot{y}_0 = 0 \quad \dot{z}_0 = \Delta V_z$$

As a result, the equations of motion become those of Equations 3.11:

$$\begin{cases} x(t) = \frac{2}{\omega} \Delta V_z (1 - \cos(\omega t)) \\ y(t) = 0 \\ z(t) = \frac{1}{\omega} \Delta V_z \sin(\omega t) \end{cases} \quad (3.11)$$

Substituting  $t = \frac{T}{2}$ , the final conditions are:

$$\begin{cases} x_f = \frac{4}{\omega} \Delta V_z \\ y_f = 0 \\ z_f = 0 \end{cases} \quad (3.12)$$

As in the tangential boost transfer, the first impulse is equal to the second, and it is determined based on the  $\Delta x$  to be achieved:  $\Delta V_{z1} = \Delta V_{z2} = \frac{\omega}{4} \Delta x$ . Therefore the total change of velocity is:  $\Delta V = |\Delta V_{z1}| + |\Delta V_{z2}| = \frac{\omega}{2} \Delta x$ . Figure 3.6 provides the trajectory resulting from this maneuver.

This maneuver is actually quasi-impulsive too, the time necessary to achieve the requested

$\Delta V$  is  $\tau = \frac{\Delta V}{\gamma_z}$ , while the set of initial conditions is:

$$x_0 = y_0 = z_0 = 0 \quad \dot{x}_0 = \dot{y}_0 = \dot{z}_0 = 0 \quad \gamma_x = \gamma_y = 0$$

Consequently, the equation of motions during boosts become:

$$\begin{cases} x(t) = \frac{2}{\omega^2} \gamma_z (\omega t - \sin(\omega t)) \\ y(t) = 0 \\ z(t) = \frac{1}{\omega^2} \gamma_z (1 - \cos(\omega t)) \end{cases} \quad (3.13)$$

The velocities during the boost are obtained by deriving the Equations 3.13:

$$\begin{cases} \dot{x}(t) = \frac{2}{\omega} \gamma_z (1 - \cos(\omega t)) \\ \dot{y}(t) = 0 \\ \dot{z}(t) = \frac{1}{\omega} \gamma_z \sin(\omega t) \end{cases} \quad (3.14)$$

The phase of free-drift is governed by the Equations 3.11, and its duration is half orbit revolution; So, in Figure 3.5  $\Delta T = \frac{T}{2}$ .

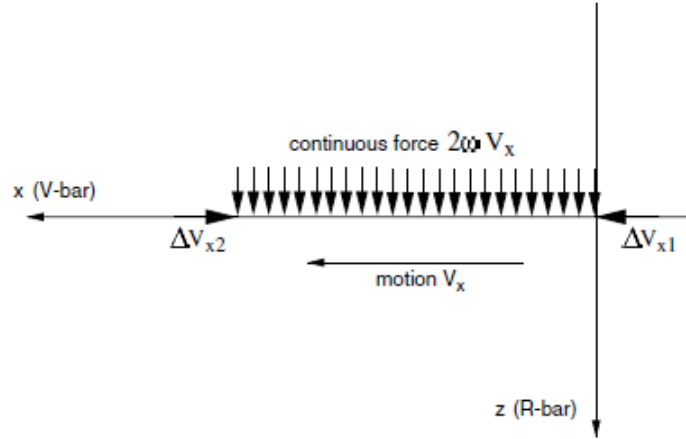


Figure 3.7: Straight line V-bar trajectory [2]

### 3.3.3 Straight line forced motion on V-bar

In this type of trajectory a constant velocity  $V_x$  is maintained between  $x_0$  and  $x_f$ , while the velocities along the other directions kept zero. It can be assumed that the motion starts with an impulse  $\Delta V_{x1} = V_x$  and then it is stopped with an opposite impulse  $\Delta V_{x2} = -\Delta V_{x1}$ .

In this case, the set of initial conditions is given by:

$$x_0 = y_0 = z_0 = 0 \quad \dot{x}_0 = V_x \quad \dot{y}_0 = \dot{z}_0 = 0 \quad \gamma_x = \gamma_y = 0$$

So the equations of motion becomes:

$$\begin{cases} x(t) = V_x \cdot t \\ y(t) = 0 \\ z(t) = 0 \end{cases} \quad (3.15)$$

From the Hill equations (3.3) is obtained that the acceleration needed to maintain this trajectory is  $\gamma_z = 2\omega V_x$ . So, the total  $\Delta V$  required to complete this maneuver is  $\Delta V = |\Delta V_{x1}| + |\gamma_z \Delta t| + |\Delta V_{x2}|$ ; where  $\Delta t = \frac{\Delta x}{V_x}$  is the duration of the maneuver, while  $\Delta x = x_f - x_0$ . The trajectory is shown in Figure 3.7.

### 3.3.4 Continuous thrust transfer along V-bar

This maneuver is very similar to that seen in subsection 3.3.2, but instead of two impulses of speed, it is achieved by a constant thrust, that produces an acceleration  $\gamma_z$  for all the duration of the maneuver.

Taking as initial conditions the following set, the equations of motion are the same of Equation 3.11.

$$x_0 = y_0 = z_0 = 0 \quad \dot{x}_0 = \dot{y}_0 = \dot{z}_0 = 0 \quad \gamma_x = \gamma_y = 0$$

Therefore, unlike the two impulses maneuver, the duration of this one is an orbital period  $T$ , so that the final conditions in Equation 3.16 are reached:

$$\begin{cases} x_f = \frac{4\pi}{\omega^2} \gamma_z \\ y_f = 0 \\ z_f = 0 \end{cases} \quad (3.16)$$

Instead, the total change of velocity is the same of the two impulses radial boost:  $\Delta V = \gamma_z T = \frac{\omega}{2} \Delta x$ . Figure 3.8 provides the trajectory of the maneuver.

### 3.3.5 Choose of the trajectory type

By comparison, it can be seen that the tangential boost maneuver is the less expensive: in the radial boost the fuel consumption is higher by a factor  $\frac{3\pi}{2}$ , the cost of the straight line approach depends on the pushing time, but it is still significantly higher than the other types, and so it is a choice to exclude.

The radial boost transfer is the best choice because of safety and operational reasons. In fact, when the first boost cannot be performed, the vehicle remains at the starter point. Instead, when the second boost fails, the chaser will return after one orbit to the starting point, looping along the trajectory ‘a’ in Figure 3.9. This allows the repetition of the transfer trajectory without extra  $\Delta V$  cost. When the first boost is interrupted prematurely,

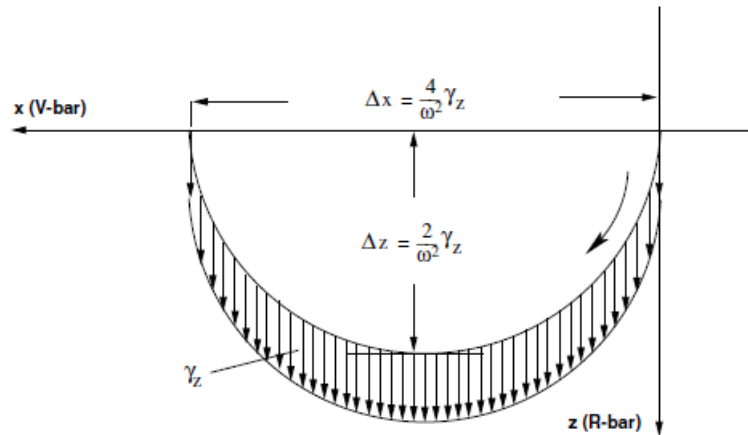


Figure 3.8: Transfer along V-bar by continuous z-thrust [2]

the motion in the x-direction up to the first return to V-bar will be shorter, the chaser loops along trajectory ‘b’. The trajectory is safe in the same way as previous case and even if the second boost is interrupted prematurely: in this case the chaser follows the trajectory ‘c’.

The tangential boost transfer cannot be regarded as equally safe. In fact, if the first or the second boost do not take place in nominal mode, the chaser could follow a trajectory that would take it to impact the target, as in trajectories ‘b’ and ‘c’ in Figure 3.10.

From the duration standpoint, the radial boost transfer offers the best result; in fact, its duration is half orbital period, while both the tangential boost and the maneuver seen in Subsection 3.3.4 have a completion time of an orbital period.

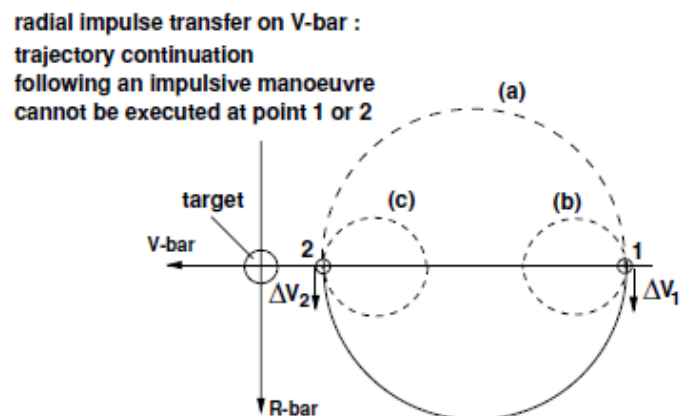


Figure 3.9: Passively safe trajectories: radial boost transfer [2]

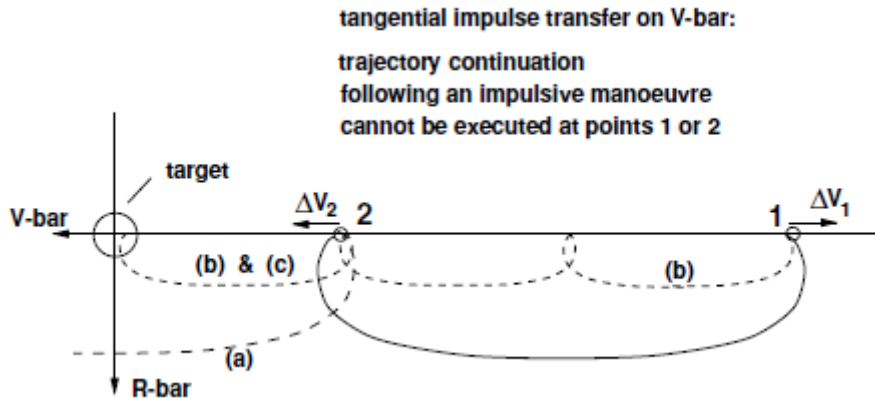


Figure 3.10: Passively safe trajectories: tangential boost transfer [2]

### 3.4 Cone of approach

During the last phase of the rendezvous and docking process, the chaser must remain within a cone of approach, following a trajectory that takes the chaser in the proximity of the docking port. The cone features are as follows:

$$r_1 = 0.75 \text{ m} \quad r_2 = 0.05 \text{ m} \quad d = 150 \text{ m} \quad \Delta h = \pm(x_f - x_1) \tan \theta + r_2$$

Figure 3.11 provides the meaning of this parameters. The start point of the trajectory inside the cone coincide with the end point of the radial boost, while the end point is 2 meters before the target.

The last part of the trajectory is a straight line approach along V-bar, while in the first part of the cone a different trajectory is followed to save fuel, as it will be shown in Chapter 6.

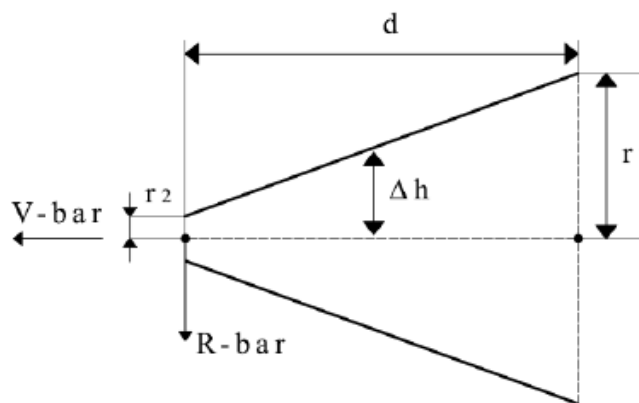


Figure 3.11: The cone of approach [7]

### 3.5 The attitude dynamic and kinematic

When the thrusters do not produce forces, the attitude dynamic is partially decoupled from the orbital dynamics, as the attitude of satellite determines the perturbative forces, therefore the orbit followed too. In any case it is always very important to know how a satellite is oriented, whether for the pointing of a payload or, as in this case, to make sure the engines get shot in the expected direction.

The aim of the attitude evaluation is to describe how the satellite is oriented, i.e. the orientation of  $F_a$  than  $F_{lo}$ . To do this there are three ways: the first uses the Direction Cosine Matrix (DMC), the second one uses the Euler angles and the last is to represent the rotation using quaternions. The definition of quaternions is based on Euler's theorem, which states that every movement of a rigid body, apart from a pure translation, can be represented by a rotation about an axis, called instantaneous axis of rotation, or Euler axis. This representation of the movement is to define the Euler axis, through the unit vector  $\vec{u} = [u_1, u_2, u_3]^T$ , and the rotation angle  $\phi$ . (Figure 3.12)

Quaternions are related to parameterization with Euler axis and angle by the following relations:

$$\begin{cases} q_1 = u_1 \sin \frac{\phi}{2} \\ q_2 = u_2 \sin \frac{\phi}{2} \\ q_3 = u_3 \sin \frac{\phi}{2} \\ q_4 = \cos \frac{\phi}{2} \end{cases} \quad (3.17)$$

From the Equations 3.17, it can be seen that:

$$q_1^2 + q_2^2 + q_3^2 + q_4^2 = 1 \quad (3.18)$$

The representation of attitude using Euler angles is easy to visualize, but computationally intense. Also a singularity problem occurs when describing attitude kinematics in terms of Euler angles and therefore it is not an effective method for spacecraft attitude dynamics. [8] Therefore, in this work, the attitude is studied using Quaternions, which are then converted into Euler angles for a view of the attitude that has a physical sense.

To obtain Quaternions, the starting point is the Euler's equation:

$$\vec{\omega}_B = I^{-1} \left[ \vec{M}_B - \vec{\omega}_B (I \vec{\omega}_B + I_{RW} \vec{\omega}_{RW}) \right] \quad (3.19)$$

Where  $\vec{\omega}_B = [p_B, q_B, r_B]^T$  is the vector of the angular speed of the chaser,  $I \in \mathbb{R}^{3,3}$  is the inertia matrix of the chaser,  $\vec{\omega}_{RW}$  and  $I_{RW} \in \mathbb{R}^{3,3}$  have the same meaning, but are related to the reaction wheels, and  $\vec{M}_B$  is the totale torque applied to the chaser. It consists of three terms, as the Equation 3.20 shows.

$$\vec{M}_B = \vec{M}_{thr} + \Delta \vec{M}_{ex} + \vec{M}_{RW} \quad (3.20)$$

Where  $\vec{M}_{thr}$  is the moment of the thrusters,  $\Delta \vec{M}_{ex}$  is the moment due to external disturbances, like the solar pressure and the effect of the gravity gradient, and  $\vec{M}_{RW}$  is the

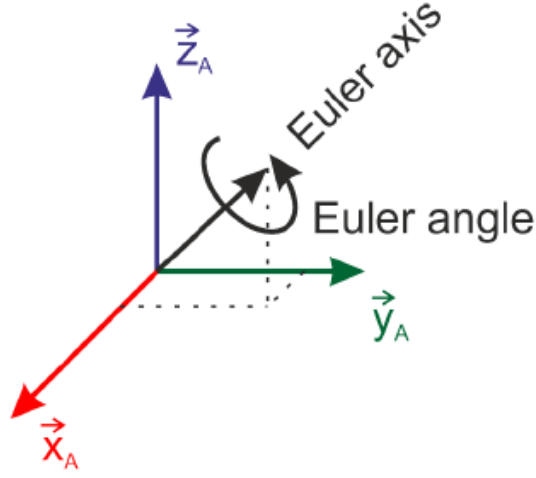


**Figure 3.12:** Euler axis and Euler angle [8]

torque provided by the reaction wheels.

From  $\vec{\omega}_B$ , the derivative of the quaternions can be calculated, as it is shown in Equation 3.21:

$$\begin{bmatrix} \dot{q}_1 \\ \dot{q}_2 \\ \dot{q}_3 \\ \dot{q}_4 \end{bmatrix} = \frac{1}{2} \begin{bmatrix} 0 & \omega_3 & -\omega_2 & \omega_1 \\ -\omega_3 & 0 & \omega_1 & \omega_2 \\ \omega_2 & -\omega_1 & 0 & \omega_3 \\ -\omega_1 & -\omega_2 & -\omega_3 & 0 \end{bmatrix} \cdot \begin{bmatrix} q_1 \\ q_2 \\ q_3 \\ q_4 \end{bmatrix} \quad (3.21)$$

Then, the quaternions are calculated through the integration of  $\dot{q}$ , and it is possible to calculate the rotation matrix  $R(q)$ , as Equation 3.22 shows:

$$R(q) = \begin{bmatrix} q_1^2 - q_2^2 - q_3^2 + q_4^2 & 2(q_1q_2 - q_3q_4) & 2(q_1q_3 + q_2q_4) \\ 2(q_1q_2 + q_3q_4) & -q_1^2 + q_2^2 - q_3^2 + q_4^2 & 2(q_2q_3 - q_1q_4) \\ 2(q_1q_3 - q_2q_4) & 2(q_2q_3 + q_1q_4) & -q_1^2 - q_2^2 + q_3^2 + q_4^2 \end{bmatrix} \quad (3.22)$$

This is the matrix that allows to rotate the forces of the thrusters, as described in Section 3.2. Furthermore, from  $R(q)$ , it is possible to derive the Euler angles, by imposing the kind of rotation. For instance, for a ‘123’ rotation, the formulas are that of Equations 3.23.

$$\begin{cases} \phi = -\arctan\left(\frac{R_{32}}{R_{33}}\right) \\ \theta = \arcsin(R_{31}) \\ \psi = -\arctan\left(\frac{R_{21}}{R_{11}}\right) \end{cases} \quad (3.23)$$

# Chapter 4

## The guidance algorithms

This chapter will first provide an overview on possible methods of robot path planning; afterwards, the technique chosen in this work will be described and analyzed.

### 4.1 Path-planning among obstacles

In recent years the issue of motion planning among obstacles assumed a great importance not only in space, but in many other areas of application. Consequently, different techniques related to this topic were developed. They are divided into four categories:

- Direct roadmap construction; the method is based on the theorem which shows that there is a semi-path clear of obstructions between each pair of configurations  $(q_{init}, q_{goal})$  if and only if there is a broken  $\tau$  contained in  $C_{free}$  (defined as the work space free of obstacles) with extremes in  $q_{init}$  and  $q_{goal}$  such that  $\tau$  vertices coincide with those of the obstacles. This method is used in particular to the computation of minimum length paths, it is one among the possible segments connecting  $q_{init}$  and  $q_{goal}$ , and passing through the vertices of the obstacles. [9], [10]
- Cell decomposition methods;  $C_{free}$  is divided into cells. If an ‘Approximate Decomposition’ is used, the union of such cells, all equal to each other, is a lower approximation of  $C_{free}$ . Instead, in the ‘Exact Decomposition’, the union of the cells is exactly  $C_{free}$ . In the first approach, any cell of the grid that intersects  $C_{obs}$  is blocked; then a path through the remaining cells is found. In the second approach to each cell is assigned a node of a graph, then two nodes are connected by an arch if cells borders. In this way the possible paths from  $q_{init}$  to  $q_{goal}$  are generated.[9], [10]
- Probabilistic roadmap; this method consists in the *pre-processing phase* and the *query phase*. During the first phase, a graph is built by placing some sampling points in the environment  $C$ ; if the graph is in  $C_{free}$ , it is added to a useful set.

In this way a roadmap is built incrementally, when the whole space is covered the second phase starts, given  $q_{init}$  and  $q_{goal}$ , they can be used as samples and tried to be connected to the graph. If connection is found a classical graph path search is conducted.[9], [10]

- Artificial potential field; in this method the robot moves under the action of a potential field  $U(q)$ . It consists of an attractive field toward the target and a repulsive field from  $C_{obs}$ . (Figure 4.1)

The desired direction is then calculated as  $-\nabla U(q)$ , where  $q$  is the position of the robot. The idea behind this method is to find a function that represents the energy of the system, and which is minimal in the position of goal. This concept was introduced for the first time by Oussama Khatib, and it is based on the physical principle of a charged particle (i.e. the robot) that moves in an electrostatic field, in which the obstacle is a charge of the same sign of the robot and the destination point is a charge of opposite sign.[10]

The APF method is suitable to the online planning: it allows to modify the potential already defined to take into account the movement of an obstacle, which can be detected by a sensor. The other three methods are better suited to offline planning.

Moreover, this method is able to plan the kinematics of the trajectory; this is a further advantage compared to other three methods, which instead solve only one aspect of looking for a geometric path.

The APF is a very attractive method, thanks to the characteristics described above and the fact of it is based on an intuitive idea. Indeed, it is the method used in this thesis to drive the chaser toward the target.

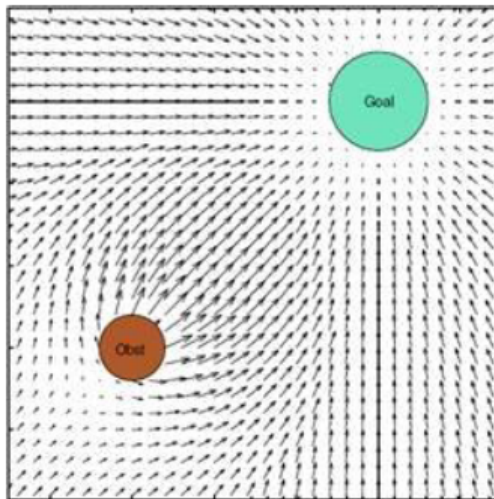


**Figure 4.1:** Attractive and repulsive forces. [11]

## 4.2 The construction of the artificial potential field

The attractive potential field towards the goal has been chosen with a parabolic profile, as in Figure 4.2. It is defined analytically from the Equation 4.1; while the corresponding attractive force is defined by Equation 4.2.

$e(q) = q_d - q$  represents the error, i.e. the difference between the desired position and the current one; while  $k_a$  is the constant of attraction.

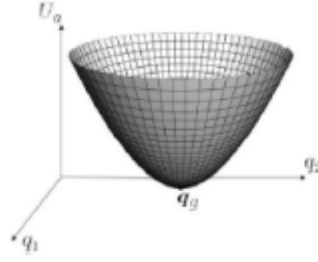


**Figure 4.2:** Parabolic potential field. [12]

$$U_a(q) = \frac{1}{2}k_a\|e(q)\|^2 \quad (4.1)$$

$$\vec{F}_a(q) = \nabla U_a(q) = k_a e(q) \quad (4.2)$$

Instead, a repulsive potential of hyperbolic profile is built around every obstacle. The Equation 4.3 provides its analytical expression.

$$U_{rep,i}(q) = \begin{cases} \frac{k_{r,i}}{\gamma} \left( \frac{1}{\eta_i(q)} - \frac{1}{\eta_{0,i}} \right)^\gamma & \text{if } \eta_i(q) < \eta_{0,i} \\ 0 & \text{otherwise} \end{cases} \quad (4.3)$$

$k_{r,i}$  is the repulsive constant,  $\gamma = 2$  is a typical choice for the hyperbolic profile,  $\eta_i(q) = \min_{q_{obs} \in CO^i} \|q - q_{obs}\|$  is the minimum distance between the chaser and the  $i$ -th obstacle,  $CO^i$  is the convex set of obstacles, and  $\eta_{0,i}$  is the distance of influence of the obstacles, i.e. maximum 300  $m$ , based on the sensor used. (Section 2.1).

In this work, a dynamic variation of the parameter  $\eta_{0,i}$  is considered, as the Equation 4.4 shows [13]:

$$R_{dyn,i} = \max \left( \eta_{0,i} + \frac{v_{r,i}|v_{r,i}|}{2\epsilon_s a_{max}}, 0 \right) \quad (4.4)$$

$v_{r,i} = (\vec{v} - \vec{v}_{obs,i}) \vec{n}_{co,i}$  is the module of relative velocity, positive if directed by the satellite toward the obstacle; in fact  $\vec{n}_{co,i}$  is the unit vector directed from the chaser to the  $i$ -th obstacle.  $\epsilon_s \in (0,1]$  is a safety factor, while  $a_{max} = \frac{u}{\sqrt{2}m_c}$  is the acceleration command;  $u$

is the output provided by the thrusters and  $m_c$  the mass of the chaser. So, the repulsive potential field becomes:

$$U_{rep,i}(q, v) = \begin{cases} \frac{k_{r,i}}{2} \left( \frac{1}{\eta_i(q)} - \frac{1}{R_{dyn,i}(q,v)} \right)^2 & \text{if } \eta_i(q) < \eta_{0,i} \text{ and } v_{r,i} > 0 \\ 0 & \text{otherwise} \end{cases} \quad (4.5)$$

The condition  $v_{r,i} > 0$  has been added in Equation 4.5. In this way the repulsive action works only if the chaser is heading to the obstacle; then  $R_{dyn}$  is calculated and used only when  $v_{r,i} > 0$ . So, taking  $\epsilon = 1$ , the dynamic range can be redefined as in Equation 4.6:

$$R_{dyn,i} = \eta_{0,i} + \frac{v_{r,i}^2}{2a_{max}} \quad (4.6)$$

$U_{rep}(p, v)$  is now a function of position and speed, the latter dependence is given by the term  $v_r$  in the expression of the dynamic radius. So, the repulsive force is given by the negative gradient of the potential field in terms of both position and velocity, as Equation 4.7 indicates.

$$F_{rep,i}(q, v) = -\nabla_q U_{rep,i}(q, v) - \nabla_v U_{rep,i}(q, v) \quad (4.7)$$

The two terms are analyzed separately:

$$\begin{aligned} \nabla_q [U_{rep,i}(q, v)] &= \nabla_q \left[ \frac{k_{r,i}}{2} \left( \frac{1}{\eta_i(q)} - \frac{1}{R_{dyn,i}} \right)^2 \right] = \\ &= -\frac{k_{r,i}}{\eta_i^2(q)} \left( \frac{1}{\eta_i(q)} - \frac{1}{R_{dyn,i}(q)} \right) \nabla_q \eta_i(q) + \\ &+ \frac{k_{r,i}}{R_{dyn,i}^2(q)} \left( \frac{1}{\eta_i(q)} - \frac{1}{R_{dyn,i}(q)} \right) \nabla_q R_{dyn,i}(q) \end{aligned} \quad (4.8)$$

The gradient of  $-\frac{1}{R_{dyn,i}}$  with respect to position is given by:

$$\begin{aligned} \nabla_q \left( -\frac{1}{R_{dyn,i}} \right) &= \frac{1}{R_{dyn,i}^2} \nabla_q (R_{dyn,i}) = \\ &= \frac{1}{R_{dyn,i}^2} \nabla_q \left( \eta_{0,i} + \frac{v_{r,i}^2}{2a_{max}} \right) = \frac{1}{R_{dyn,i}^2} \frac{v_{r,i}}{a_{max}} \nabla_q (v_{r,i}) \end{aligned} \quad (4.9)$$

At this point the Equation 4.10 is inserted [14]:

$$\nabla_q [v_{r,i}(q)] = -\frac{1}{\eta_i(q)} v_{r\perp,i} \vec{n}_{co\perp,i} = -\frac{1}{\eta_i(q)} (\vec{v} - \vec{v}_{obs,i} - v_{r,i} \vec{n}_{co,i}) \quad (4.10)$$

Where  $v_{r\perp,i}$  is the module of the component of the relative velocity of the chaser with respect to the  $i$ -th obstacle which is perpendicular to the line passing through the chaser

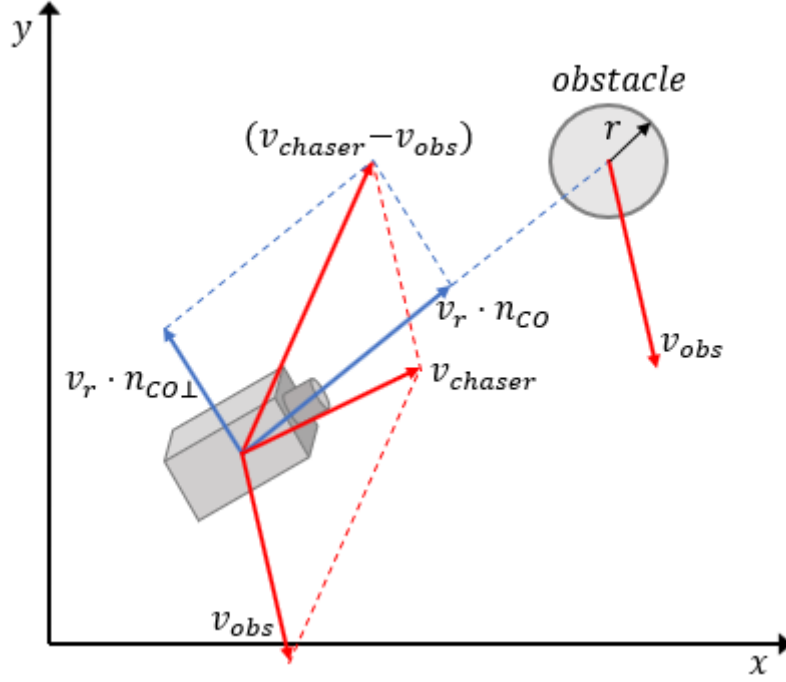


**Figure 4.3:** Relations among the vectors velocities.

and the  $i$ -th obstacle, and  $\vec{n}_{co\perp,i}$  is the corresponding unit vector. Figure 4.3 clarifies the relations among vectors velocities used in the Equation 4.10.

So the Equation 4.9 becomes:

$$k_{r,i} \left( \frac{1}{\eta_i(q)} - \frac{1}{R_{dyn,i}} \right) \frac{1}{R_{dyn,i}^2} \frac{v_{r,i}}{a_{max}} \left( -\frac{1}{\eta_i(q)} \right) (\vec{v} - \vec{v}_{obs,i} - v_{r,i} \vec{n}_{co,i}) \quad (4.11)$$

Then Equation 4.8 can be rewritten as:

$$\begin{aligned} \nabla_q [U_{rep,i}(q, v)] &= \\ &= -\frac{k_{r,i}}{\eta_i^2(q)} \left( \frac{1}{\eta_i(q)} - \frac{1}{R_{dyn,i}} \right) \vec{n}_{co,i} + \\ &+ \frac{k_{r,i}}{R_{dyn,i}^2} \left( \frac{1}{\eta_i(q)} - \frac{1}{R_{dyn,i}} \right) \frac{v_{r,i}}{a_{max}} \left( -\frac{1}{\eta_i(q)} \right) (\vec{v} - \vec{v}_{obs,i} - v_{r,i} \vec{n}_{co,i}) \end{aligned} \quad (4.12)$$

Now the gradient of the potential field in terms of velocity is analyzed:

$$\begin{aligned} \nabla_v [U_{rep,i}(q, v)] &= \nabla_v \left[ \frac{k_{r,i}}{2} \left( \frac{1}{\eta_i(q)} - \frac{1}{R_{dyn,i}} \right)^2 \right] = \\ &= \frac{k_{r,i}}{R_{dyn,i}^2(v)} \left( \frac{1}{\eta_i} - \frac{1}{R_{dyn,i}(v)} \right) \nabla_v R_{dyn,i}(v) \end{aligned} \quad (4.13)$$

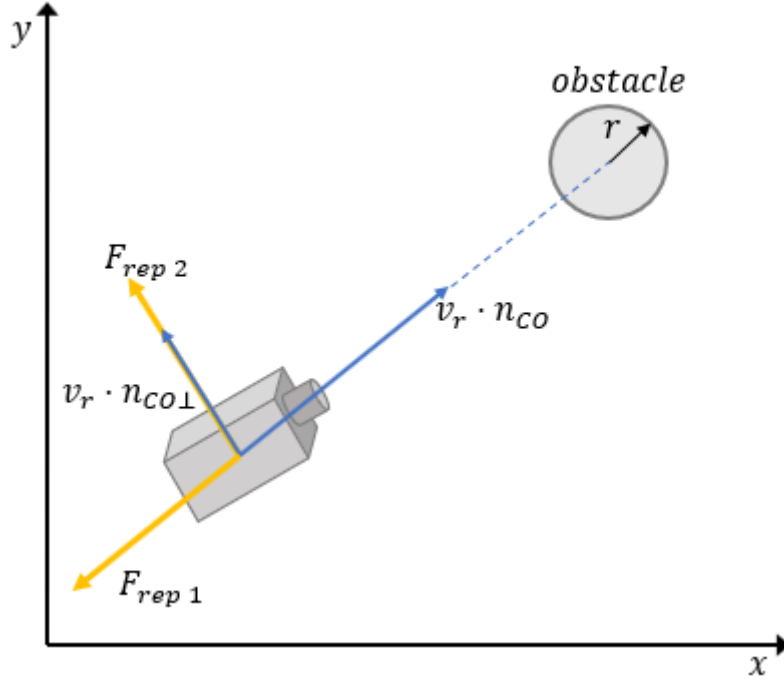


Figure 4.4: Repulsive forces.

The gradient of  $-\frac{1}{R_{dyn,i}}$  with respect to velocity is given by:

$$\begin{aligned} \nabla_v \left( -\frac{1}{R_{dyn,i}} \right) &= \frac{1}{R_{dyn,i}^2} \nabla_v (R_{dyn,i}) = \\ &= \frac{1}{R_{dyn,i}^2} \nabla_v \left( \eta_{0,i} + \frac{v_{r,i}^2}{2a_{max}} \right) = \frac{1}{R_{dyn,i}^2} \frac{v_{r,i}}{a_{max}} \nabla_v (v_{r,i}) \end{aligned} \quad (4.14)$$

And since  $\nabla_v [v_{r,i}(v)] = \vec{n}_{co,i}$  [14], Equation 4.13 becomes:

$$\nabla_v [U_{rep,i}(q, v)] = k_{r,i} \left( \frac{1}{\eta_i(q)} - \frac{1}{R_{dyn,i}} \right) \frac{1}{R_{dyn,i}^2} \frac{v_{r,i}}{a_{max}} \vec{n}_{co,i} \quad (4.15)$$

So the repulsive force is obtained by changing sign and adding the Equations 4.12 and 4.15; it has two components:  $\vec{F}_{rep,i} = \vec{F}_{rep 1,i} + \vec{F}_{rep 2,i}$ .

$$\begin{aligned} \vec{F}_{rep 1,i} &= -k_{r,i} \left( \frac{1}{\eta_i(q)} - \frac{1}{R_{dyn,i}} \right) \left( -\frac{1}{\eta_i^2(q)} \right) \vec{n}_{co,i} + \\ &\quad - k_{r,i} \left( \frac{1}{\eta_i(q)} - \frac{1}{R_{dyn,i}} \right) \frac{1}{R_{dyn,i}^2} \frac{v_{r,i}}{a_{max}} \vec{n}_{co,i} \end{aligned} \quad (4.16)$$

$$\vec{F}_{rep 2,i} = -k_{r,i} \left( \frac{1}{\eta_i(q)} - \frac{1}{R_{dyn,i}} \right) \frac{1}{R_{dyn,i}^2} \frac{v_{r,i}}{a_{max}} \left( -\frac{1}{\eta_i(q)} \right) (\vec{v} - \vec{v}_{obs,i} - v_{r,i} \vec{n}_{co,i}) \quad (4.17)$$

Figure 4.4 shows that the component  $\vec{F}_{rep\ 1,i}$  is directed along the line joining chaser-obstacle, and it reduces the value of the relative speed  $v_{r,i}$ . The other component  $\vec{F}_{rep\ 2,i}$  increases the component of relative velocity  $v_{r\perp,i}$ , and will act as a steering force for detouring. [14]

The overall potential is the sum of individual potential, as the Equation 4.18 and the Figure 4.5 show.

$$U_{tot}(q, v) = U_a(q) + \sum_{i=1}^{n\ obs} U_{rep,i}(q, v) \quad (4.18)$$

Thus, the total force that moves the satellite toward the goal avoiding obstacles is given by Equation 4.19. Later this force is normalized in order to know the exact direction that the chaser must follow. (Equation 4.20)

$$\vec{F}_{tot} = \nabla U_{tot}(q, v) = \vec{F}_a + \sum_{i=1}^{n\ obs} \vec{F}_{rep\ 1,i} + \sum_{i=1}^{n\ obs} \vec{F}_{rep\ 2,i} \quad (4.19)$$

$$E_U = \frac{F_{tot}}{\|F_{tot}\|}. \quad (4.20)$$

Finally, once the value of the speed  $\dot{x}_{max}$  is fixed for each part of rendezvous maneuver, the desired velocity of the Chaser is equal along the three axes. (Eq. 4.21)

$$\dot{x}_d = \dot{x}_{max} E_U, \in \mathbb{R}^3 \quad (4.21)$$

where  $\dot{x}_{max}$  is defined in accordance to the desired performance.

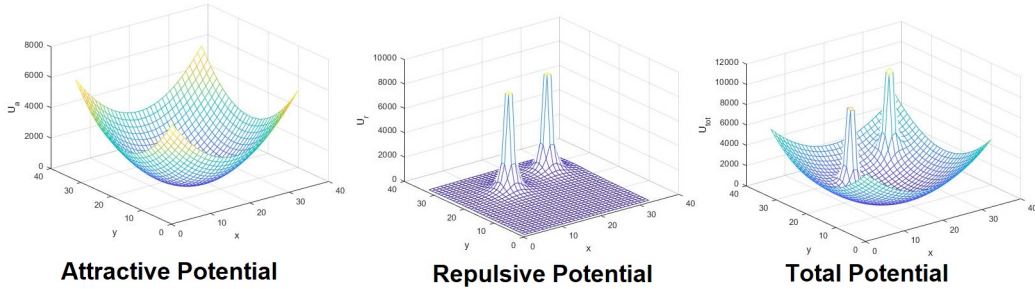


**Figure 4.5:** Total potential field.



# Chapter 5

## The control strategy

A control system establishes a relationship between an input variable (called "reference") and an output variable, which is then controlled; The control can only occur in a temporal regime.

This chapter provide the information about the techniques used in this thesis to ensure the managing of both the position and the attitude of the chaser. To regulate both of these parameters, the methodology used is that of the Sliding Mode Control (SMC). It is a Variable Structure Control (VSC) method, which changes the dynamics of a system through the actuation of a high frequency control signal. This command forces the system to reach a *sliding surface*, which represents the reference of the control system. Since the frequency of the control signal is not infinite, the trajectories of the system will oscillate around the sliding surface. This phenomenon is called *chattering*, and the higher the frequency, the more it is attenuated.

the VSC methods are characterized by feedback control laws and by a rule of decision,

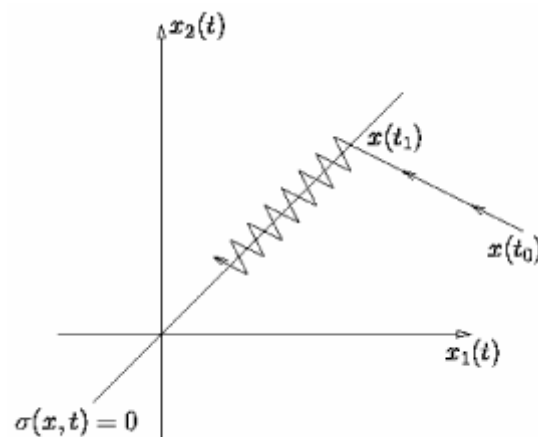


**Figure 5.1:** The chattering phenomenon near a sliding surface [15]

that is called *switching function*. The latter has as inputs some measurements of the current behavior of the system and provides as output the feedback control that the system must adopt. The main purpose of this control system is to lead, and then maintain, the system status close to the desired location, where the switching function intervenes. The design for this type of control systems consists of selecting two components: one is the switching function, while the other is the control law, that must ensure that the region where the switching function intervenes is attractive for the system.

The main advantage of this technique is its robustness, due to a low sensitivity to plant parameter uncertainty. In addition, the control system does not follow a continuous function, so that the equilibrium is achieved in a finite time; that is better than an asymptotic behaviour.

The SMC is particularly suited to this work, because it is a nonlinear controller and also the dynamics of the problem is nonlinear.

Proposed control algorithms require a minimum computational cost, and for this they are easily implementable successfully on-board.

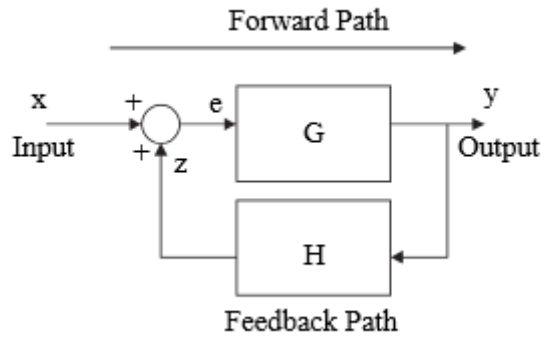


Figure 5.2: Feedback system

## 5.1 First order Sliding Mode to position control

Having regard to the nature of the thrusters, to control the position of chaser it is used a first-order sliding mode controller. In fact, these provide a boost which cannot be continuously modulated, but they can only be accessed, providing the maximum boost, or powered off.

The Hill equations (Equations 3.3) can be rewritten as follows:

$$\ddot{x} = A_x(x, \dot{x}) + \Delta_x + B_x u_x + \Delta_u \quad (5.1)$$

Where  $A_x(x, \dot{x}) \in \mathbb{R}^{3,3}$  is the array of the spacecraft dynamics,  $\Delta_x = \frac{1}{m_c} \Delta F_{ex} \in \mathbb{R}^3$  is the vector of the external disturbances,  $B_x = \frac{1}{m_c} I_3 \in \mathbb{R}^{3,3}$  is the control matrix,  $\Delta_u \in \mathbb{R}^3$

is the vector of thrusters errors, and  $u_x \in \mathbb{R}^3$  is the nominal forces exerted by the thrusters. To compute the latter vector, the SMC uses the Equation 5.2

$$u_x = -B_x^{-1} \cdot K \cdot \text{sign}(\sigma_x) \quad (5.2)$$

Where  $K = n \cdot T_{max}$  and  $n = 2$ , i.e. the maximum number of thrusters that can be switched on simultaneously for each direction of thrust. Instead,  $\sigma_x$  is the output of the control law. (Equation 5.3)

$$\sigma_x = (\dot{x} - \dot{x}_d) + c_x(x - x_d) \quad (5.3)$$

$x, \dot{x} \in \mathbb{R}^3$  are respectively the position and velocity vectors,  $x_d \in \mathbb{R}^3$  is the position of the goal and  $\dot{x}_d$  is the desired velocity of the chaser. Finally,  $c_x \in \mathbb{R}^3$  is a constant, and it is choice positive.

## 5.2 Super-twisting Sliding Mode to attitude control

This technique is proposed for attitude control through the reaction wheels and it is a continuous-action control, without limitation of frequency.

Considering the dynamic system:

$$\dot{x} = A(t) + B(t)u \quad (5.4)$$

The positive constants  $C, K_m, K_M, U_M, q$  must meet the following conditions:

$$\left| \dot{A} \right| + U_M \left| \dot{B} \right| \leq C, \quad 0 \leq K_m \leq B(t) \leq K_M, \quad \left| \frac{A}{B} \right| < qU_M, \quad 0 < q < 1$$

The Super-twisting controller implements the following equation:

$$u = -\lambda \cdot |\sigma|^{1/2} \cdot \text{sign}(\sigma) + u_1 \quad (5.5)$$

Where  $u$  is the control action, while  $u_1$  is:

$$\dot{u}_1 = \begin{cases} -u & \text{if } |u| > U_M \\ \alpha \text{sign}(\sigma) & \text{if } |u| \leq U_M \end{cases} \quad (5.6)$$

With  $K_m \alpha > C$  and  $\lambda$  sufficiently large, the controller guarantees the appearance of a 2-sliding mode  $\sigma = \dot{\sigma} = 0$ , which attracts the trajectories in finite time. The control  $u$  enters in finite time the segment  $[-U_M, U_M]$  and stays there. It never leaves the segment, if the initial value is inside at the beginning.[16]

A sufficient condition for validity of this affirmation is:

$$\lambda > \sqrt{\frac{2}{(K_m \alpha - C)} \frac{(K_m \alpha + C) K_M (1 + q)}{K_m^2 (1 - q)}} \quad (5.7)$$

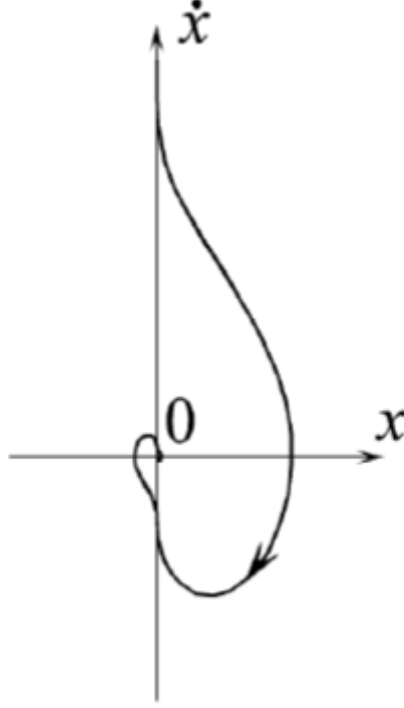


**Figure 5.3:** Trajectory of the super-twisting controller [16]

In this thesis, the actuation system consists of the reaction wheels, whose angular speeds are computed by means of the Euler equation (Equation 3.19), that could be rewritten as follows:

$$\dot{\omega}_B = A_\omega(\omega_B, \omega_{RW}) + \Delta_\omega + \Delta_{\omega \text{ thr}} + B_\omega u_\omega \quad (5.8)$$

Where  $\Delta_\omega = -I^{-1}\Delta M_{ex} \in \mathbb{R}^3$  is the vector of the external disturbances,  $\Delta_{\omega \text{ thr}} = -I^{-1}\Delta M_{thr} \in \mathbb{R}^3$  is due to the errors of the thrusters,  $B = -I^{-1} \in \mathbb{R}^{3,3}$  is the control array, and  $u_\omega \in \mathbb{R}^3$  is the vector of the momentum exerted by the reaction wheels. The latter is defined in accordance with the algorithm STW sliding mode as follows:

$$u_\omega = -\lambda \cdot |\sigma_\omega|^{1/2} \cdot \text{sign}(\sigma_\omega) + v_\omega \quad (5.9)$$

In which  $v_\omega$  is:

$$v_\omega = \begin{cases} -u_\omega & \text{if } |u_\omega| > U_M \\ \alpha \text{ sign}(\sigma_\omega) & \text{if } |u_\omega| \leq U_M \end{cases} \quad (5.10)$$

A saturation value is taken into account for the reaction wheel: if the computed command is greater than 1 Nm then  $u_\omega$  is cut down.

Instead,  $\sigma_\omega$ , i.e. the output of this controller, is defined as follow:

$$\sigma_\omega = \omega_B + C_\omega \delta q_{13} \quad (5.11)$$

Whith  $C_\omega \in \mathbb{R}^{3,3}$  is a positive defined matrix; while  $\delta q_{13}$  is based on the desired attitude  $q_d = [0,0,0,1]$ , i.e. the body frame is aligned to LVLH frame. (Equation 5.13)

$$\delta q_{13} = \Sigma^T(q_d) \cdot q \quad (5.12)$$

$\Sigma(q_d)$  is a matrix with the following structure:

$$\Sigma(q_d) = \begin{bmatrix} q_4 I_3 + Q_{13} \\ -q_{13}^T \end{bmatrix} \quad (5.13)$$

Where  $Q_{13}$  is:

$$Q_{13} = \begin{bmatrix} 0 & -q_3 & -q_2 \\ q_3 & 0 & -q_1 \\ -q_2 & q_1 & 0 \end{bmatrix} \quad (5.14)$$



# Chapter 6

## Simulations and results

### 6.1 The simulation scenario

As mentioned earlier, the objective of this thesis is to simulate a rendezvous and docking maneuver, implementing a control strategy for the 6 degrees of freedom of the chaser, i.e. position and attitude, and a guidance law based on artificial potential field (APF).

It is assumed that the origin of LVLH reference system coincides with the center of mass of the target, and that at the initial time the chaser is distant from it about  $3 \text{ km}$ . Table 6.1 provides the features of the chaser, of the initial orbit and of the two obstacles with which the chaser interacts during the radial boost.

Using the Hill equations to include the orbital dynamics, the approach maneuver has been studied by dividing it into two phases: the radial boost and the cone of approach, as Figure 6.1 shows. The docking dynamic, that is usually analyzed with dynamic of multibody systems, it is not here considered; So the simulation is stopped when the chaser is 2 metres away from the target.

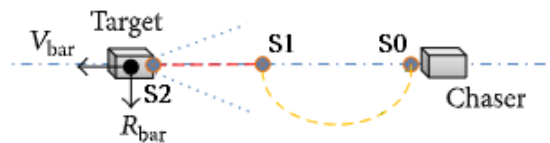


Figure 6.1: The two phases of the approach maneuver [6]

In this work, it has been tested that the guidance algorithm is capable to lead the chaser to the desired end position of the radial boost with a fine tolerance, i.e.  $x = -200 \text{ m}$ ,  $y = z = 0$ . However, to simulate a more realistic scenario, the radial boost is stopped when the  $x$  coordinate reaches a value that is 10 meters away from that desired, i.e.  $x = -200 \text{ m}$ , and the corresponding values of position and speed of the chaser are used as input for the

last phase of approach. Table 6.2 provides the initial conditions for the two phases of the maneuver.

In order to explain the process followed in the simulation of the two maneuvers, the second and third block are decomposed into additional blocks, as Figure 6.3 shows.

Parameter	Value	Unit of measure
Initial mass of the chaser	600	<i>kg</i>
Initial inertia tensor of the chaser	$144 \cdot I_3$	<i>kg · m<sup>2</sup></i>
Orbital height	500	<i>km</i>
Thrust nominal	1	<i>N</i>
Specific Impulse nominal	220	<i>s</i>
Zero shot time of the thrusters	$20 \cdot 10^{-3}$	<i>s</i>
Maximum torque of the reaction wheels	1	<i>N · m</i>
Inertia tensor of the reaction wheels	$0.1 \cdot I_3$	<i>kg · m<sup>2</sup></i>
Obstacle detection range	300	<i>m</i>
Radius of the obstacles	50	<i>m</i>
Starting position of obstacle 1	$[-2400, 100, 15]$	<i>m</i>
Speed of obstacle 1	$[-0.5, -0.08, 0.02]$	<i>m/s</i>
Starting position of obstacle 2	$[-1430, -50, -500]$	<i>m</i>
Speed of obstacle 2	$[0.15, 0.03, 0.3]$	<i>m/s</i>

**Table 6.1:** Features of the chaser, of the initial orbit and of the obstacles.

Phase	Initial conditions	Unit of measure
Radial Boost	$x_0 = -3; y = z = 0$	<i>km</i>
	$\dot{x}_0 = \dot{y}_0 = \dot{z}_0 = 0$	<i>m/s</i>
S2-S3	$\phi = 0.2 \theta = 0.5 \psi = 0$	<i>rad</i>
	$\dot{\omega}_B = [0, 0, 0]$	<i>rad/s</i>
Cone of Approach	$x_0 = -210; y, z$ from Hill equations	<i>m</i>
	$\dot{x}_0, \dot{y}_0, \dot{z}_0$ from Hill equations	<i>m/s</i>
S3-S4	$\phi, \theta, \psi$ from Euler equation	<i>rad</i>
	$\dot{\omega}_B$ from Euler equation	<i>rad/s</i>

**Table 6.2:** The conditions of the chaser at the initial time of the two phases

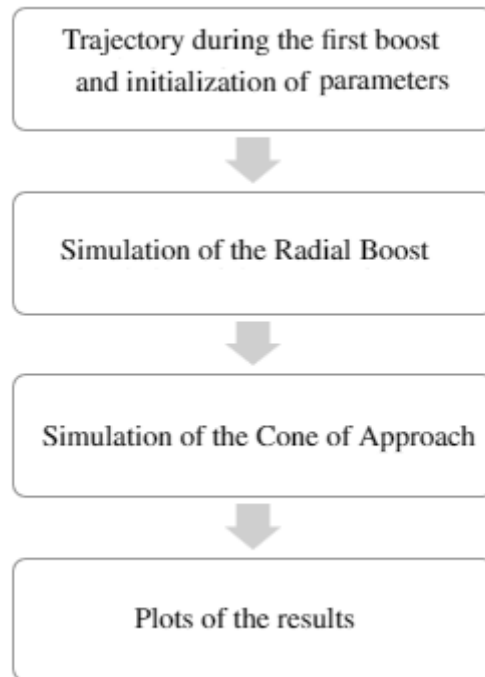


**Figure 6.2:** Logical process of the Matlab code

## 6.2 The Matlab code

For the simulation of the maneuver, the software Matlab has been used. It is an excellent tool to simulate the behavior of a system that varies over time according to precise mathematical models.

Within this program the equations described in the previous sections are implemented. The code is divided into two parts: the first is related to the radial boost, then the output of this are used as inputs for the cone of approach. In addition to this, there is an initial part where the trajectory during the first boost is calculated using Equations 3.13 and 3.14 and where the various parameters are initialized, such as the coordinates of the goal and the position and speed of the obstacles. Finally, there is a part that generates the plot of the results obtained. This is summarized in Figure 6.2.

The cycle of Figure 6.3 is repeated using a *while* cycle until the coordinate  $x$  reaches the value of  $-210\text{ m}$  for the radial boost, and then again it repeats itself at the stage of final approach until the chaser reaches  $x = -2\text{ m}$ .

Below, the operations carried out within several blocks of Figure 6.3 are explained in detail, as well as the refresh rate and the relationships between them.

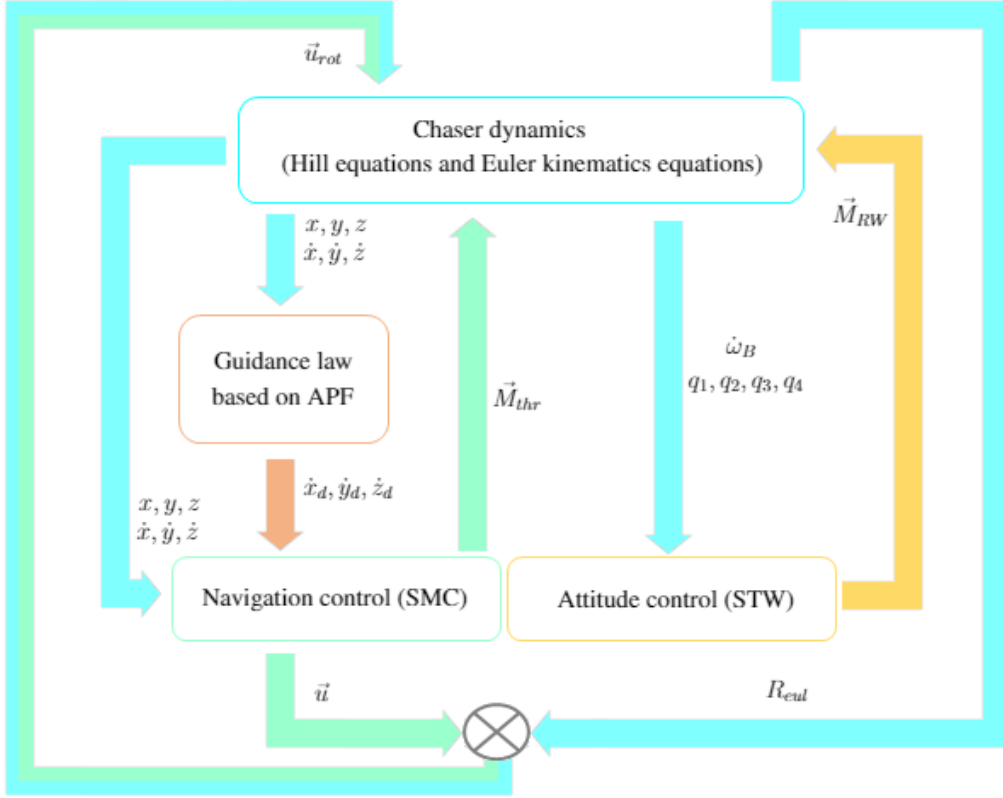


Figure 6.3: Matlab model for the simulation of the maneuvers

### 6.2.1 The block of the Chaser dynamics

The update frequency of this block is  $100 \text{ Hz}$ , and inside it, operation concerning both the guidance that the attitude are carried out.

Regarding the position dynamics, in this block the Hill equations (Equations 3.3) are integrated using the integrator *ode45*. For this operation, the integrator receives in input the accelerations  $\vec{u}_{rot}$  provided by the control system and suitably rotated in LVLH reference system, using the information on the attitude. By means of the integration, the position and speed of the chaser are obtained, they are used within other blocks as it will be explained later.

To fulfill the attitude function, the momentum provided by the reaction wheels  $\vec{M}_{RW}$  and the torque generated by the thrusters  $\vec{M}_{thr}$  are required. The latter is caused by the difference between the boost provided by the two actuators that point in the same direction, due to errors, and this difference generates a torque, although it should be nominally null. Given these inputs,  $\dot{q}$  is calculated by using Equations (3.19), (3.21). Then, it is integrated using the integrator *ode45* to obtain the quaternions  $q$ , which are the inputs for the attitude control. In addition, quaternions produces both Euler angles, using the Matlab function

*DCM2angle* and specifying the rotation *123*, and the rotation matrix  $R_{eul}$  with the Matlab function *quat2DCM*. [17]

Also, within this block the mass value of the satellite is updated, using the Equation 6.1, which is integrated with *ode45* and where  $n$  depends on the number of thrusters on during that time step.

$$\dot{m}_c = -\frac{nT_{max}}{g_0 I_{sp}} \quad (6.1)$$

### 6.2.2 The block of the Guidance law

The update frequency of this block is 1 *Hz*, it receives as input the current values of both position and speed of the chaser, which are used as shown in Chapter 4 to obtain the direction of the desired velocity  $[\dot{x}_d, \dot{y}_d, \dot{z}_d]$ .

Because the sensor is able to detect the location of the obstacle only if it is less than 300 meters, an *if* cycle is used so that if the distance is greater, the satellite is affected only the attractive force (Equation 4.2). This situation comes even if the obstacle is in the range of detection but the relative velocity between chaser and target is less than zero,  $v_r < 0$ , because in this case the Chaser is moving away from the obstacle and no repulsive action is needed.

Otherwise, the chaser is influenced by both the attraction and the repulsive action, and the latter is calculated by entering both the speed of the obstacle and the position of the same, that is calculated as the starting position is known, in the Equations (4.16), (4.17).

In the cone approach phase no obstacles are included, so there is only the attraction part of the potential field. However, it is changed compared to that used in radial boost: when  $x < -100$  *m*, through the *if* cycle, the desired speed along  $z$  is set equal to the  $z$ -component of the current velocity if the  $z$  coordinate of the chaser is less than the 85% the value of the cone  $z$  value. Besides, the attractive force is calculated by weighing the contribution in  $z$  with one fact for 100. This means that, when the chaser reaches the limits of the cone, the desired speed will be mainly in the  $z$ -direction, then the chaser is brought back toward the axis of the cone by the thrusters. In this way, in the first part of the cone the chaser follows a trajectory to half-waves, as it will be shown in Subsection 6.3.2, and fuel is saved. Instead, in the last 75 meters, the attractive force is computed as in the radial boost, and the *if* cycle on the  $z$  coordinate is deleted, then the satellite follows a straight-line approach along  $\bar{V}$ .

### 6.2.3 The block of the position control

The update frequency of this block is 10 *Hz*. Inside it, the equations of Section 5 are implemented, in order to derive the forces  $\vec{u}$  that the actuators must carry to pursue the desired trajectory.

To perform its function, this block requires of the position and speed of the chaser (provided by the block of the Chaser dynamics), the desired speed (provided by the block of

the APF), and the coordinates of goals, which are known and that depend on the phase of the maneuver.

Because the  $y$  coordinate oscillates around zero for the entire maneuver, an *if* cycle is implemented, so if  $|y - y_d|$  is less a tolerance value, it is imposed that  $F_y = 0$ . The tolerance is set at  $10^{-2}$  in the radial boost and at  $10^{-3}$  in the cone. Since during the latter part of the cone also the  $z$  coordinate oscillates around zero, the same control is performed for it during this stage.

Additionally, within this block  $\vec{M}_{thr}$  is calculated, which is explained in Subsection 6.2.1. To do this, the nominal thrust of each of 2 thrusters that should give thrust in one direction is changed by introducing a *random* error and an error *bias*; then the resultant moment is computed taking into account the configuration of the chaser. (Figure 2.3)

#### 6.2.4 The block of the Attitude control

The update frequency of this block is 1 Hz. It receives as input both the derivative of the angular velocity of the chaser  $\vec{\omega}_B$  and the quaternions  $q$ ; then the equations of Chapter 5 are implemented and the moments of the reaction wheels  $\vec{M}_{RW}$  are computed.

In order to respect the constraint on the maximum momentum provided, an *if* cycle is constructed so that if the value that comes out of the equations is greater than 1 Nm, it is cut down.

#### 6.2.5 Real effects

In order to make the simulation of the maneuver more realistic, the dynamics of the thrusters and the orbital disturbances were introduced within the matlab code.

As regards the first aspect, a low-pass filter has been applied to the square wave signal representing the ideal command. Figure 6.4 provides both the evolution of the trust over time and the formula used to create this filter; ‘E’ is  $T_{max}$  and ‘RC’ is set equal to  $10^{-3}$  s since the transient of the thrusters is on the order of microseconds.

Instead, orbital disturbances were estimated on the basis of both the orbital altitude and the size of satellite. The aerodynamic drag acts only along V-bar, using the classic Equation 6.2, it has been calculated that is on the order of  $10^{-4}$  N. The force due to the ‘J2’ effect is inserted as random value, on the order of  $10^{-6}$  N; while the effect of the solar pressure produces both a constant force in the order of  $10^{-7}$  N and a constant torque in the order of  $10^{-6}$  Nm. Finally, on the basis of the height of the orbit and the size of the satellite it has been estimated that the value of the moment due to the gravitational effect is in the order of  $10^{-3}$  Nm.

$$F_D = \frac{1}{2} \rho C_D A V_x^2; \quad (6.2)$$

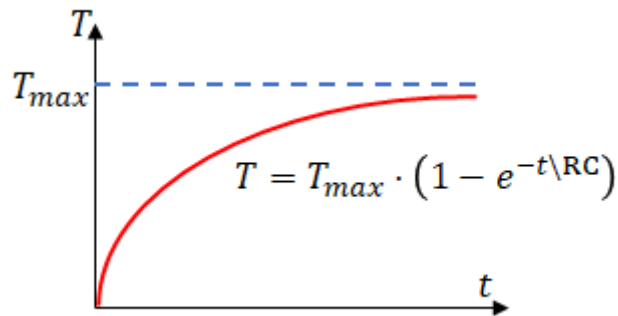


**Figure 6.4:** Evolution of the trust over time

### 6.3 Simulation results

This section provides the most significant results obtained in this thesis. Figure 6.5 shows the trajectory of the complete maneuver in the  $xz$  plane, with two moving obstacles in the radial boost maneuver; while Figure 6.6 provides the trajectory in the  $xy$  plane.

The various ‘x’ markers along the trajectory are representative of significant positions of the chaser during the obstacle avoidance, as it will be explained in Subsection 6.3.1. While the asterisk cyan marks the division between the radial boost and the phase of the cone approach, which ends at the cyan circle and that is described in Subsection 6.3.2.

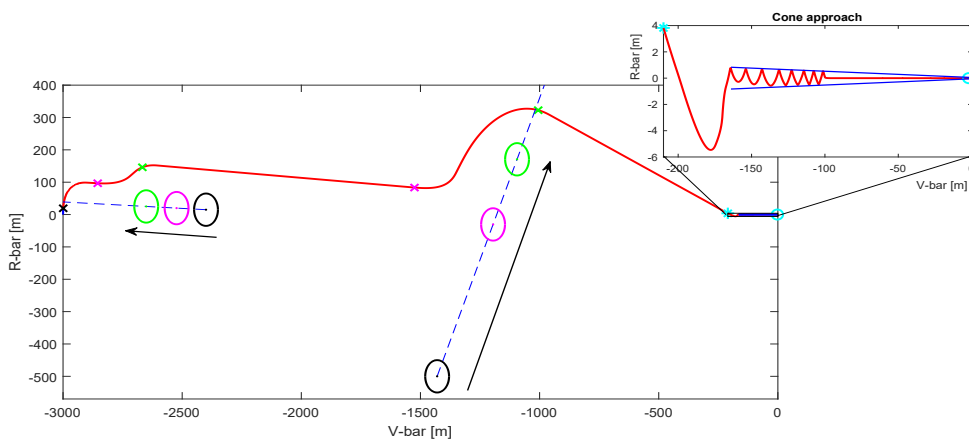


**Figure 6.5:** Trajectory of chaser in the  $xz$  plane during the maneuver

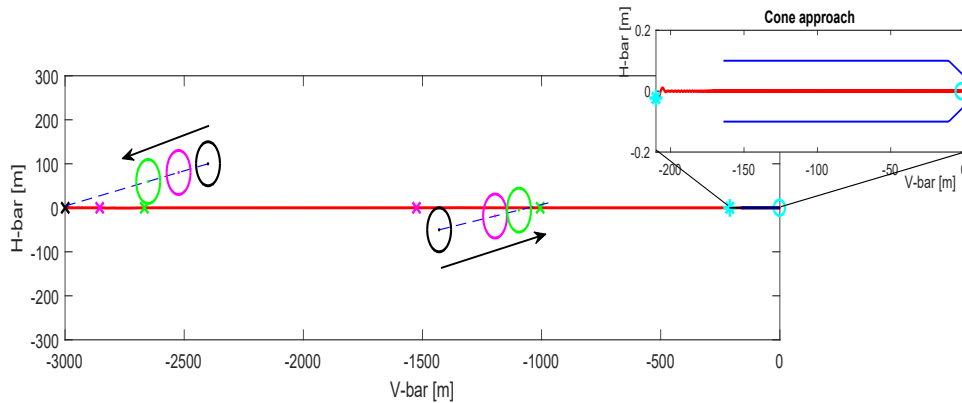


**Figure 6.6:** Trajectory of chaser in the  $xy$  plane during the maneuver

### 6.3.1 The radial boost with two obstacles

This subsection provides main results obtained during the Radial Boost phase, in terms of:

- Trajectory in the  $xz$  and  $xy$  plan,
- Speed of the Chaser,
- Forces provided by thrusters,
- Moment exerted by reaction wheels,
- Angular velocities,
- Euler angles,
- Quaternions,
- Sliding Mode surface.

As Figure 6.7 shows, the chaser avoids obstacles and arrives near the desired end position, but the simulation is stopped before the satellite can reach it, in order to simulate a scenario where the guidance system fails to achieve the desired position with large accuracy.

The black 'x' on the trajectory marks the point where the Chaser achieve the initial  $\Delta V$  to perform the Radial Boost maneuver. The arrows indicate the direction in which the obstacles are moving, while the circles identify the section of the obstacle in the plane. As it is possible to see, they are presented in three different colors:

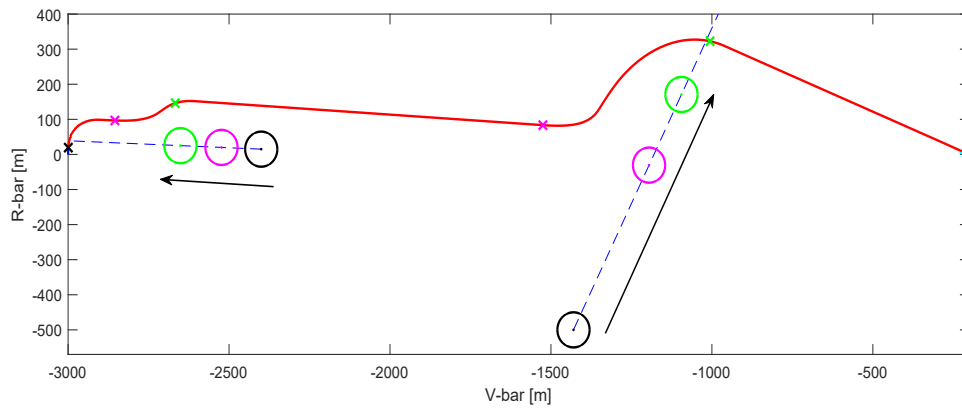


**Figure 6.7:** Trajectory of chaser in the  $xz$  plane during the radial boost

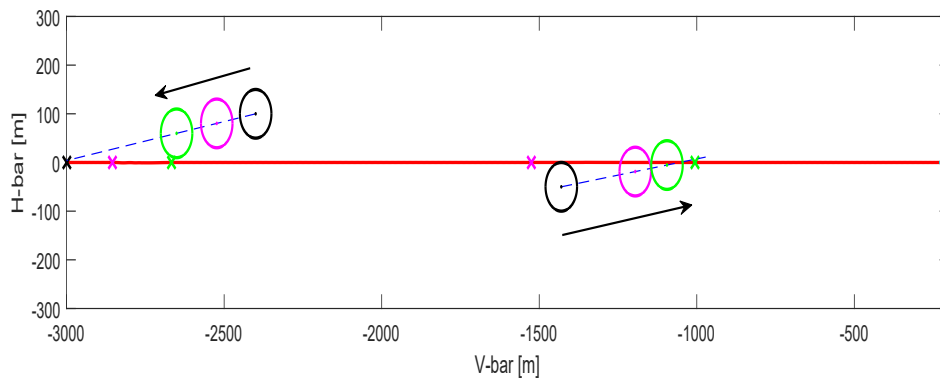


**Figure 6.8:** Trajectory of chaser in the  $xy$  plane during the radial boost

- The black one indicates the initial position of the obstacle, the black 'x' in the path identifies the location of the chaser at the same time.
- The magenta circle identify the position of the obstacle when the chaser detects its presence. When this situation occurs, the position of the chaser is indicated by a magenta 'x' marker.
- The green circle shows the position of the obstacle when the chaser is out of its range of influence. The position of the chaser at this time is marked by a green 'x' on its trajectory.

Focusing on Figure 6.8, it seems that the chaser impacts obstacles. This does not really happen because the avoidance is made along the  $z$  coordinate, as Figure 6.7 shows. This

strategy was chosen to prevent the satellite out of the plane  $y = 0$ . For the radial boost, the consumption is  $7.35 \text{ kg}$  of propellant.

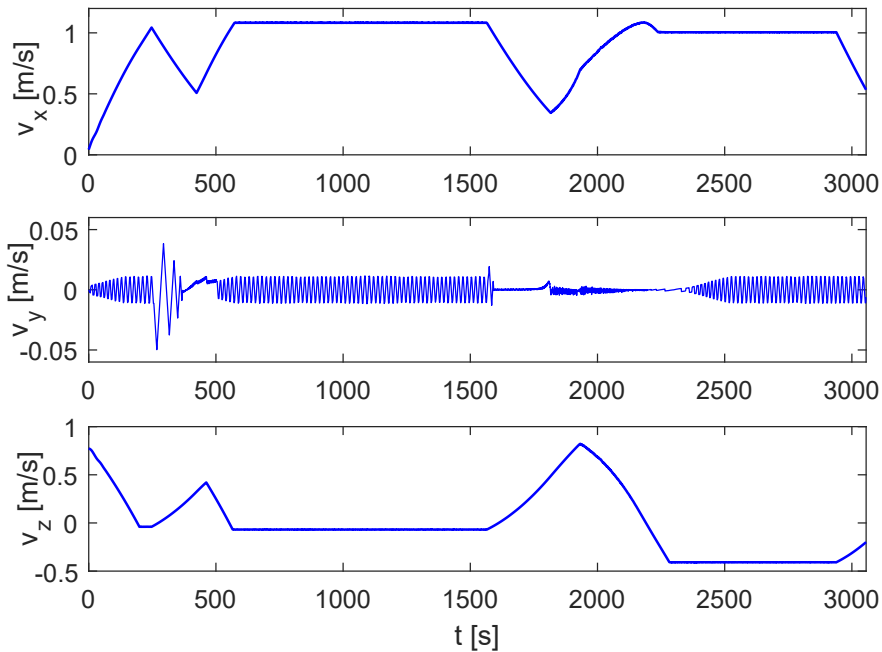


**Figure 6.9:** Speed during radial boost

Figure 6.9 shows that the value of the component  $v_y$  of the speed fluctuates around zero, the maximum amplitude is about  $10^{-2} \text{ m/s}$ , whereas the  $v_z$  component starts with a value that is given by the initial impulse of the radial boost, then it undergoes a change in proximity of obstacles, as well as the component along  $x$ . During the last part of the maneuver, the absolute value of both  $v_x$  and  $v_z$  drop. This is due because the desired speed is decreased to allow the satellite to enter in the cone approach. At the end of the maneuver the velocity in  $x$  is approximately  $0.65 \text{ m/s}$ , while the velocity in  $z$  is  $-0.15 \text{ m/s}$ .

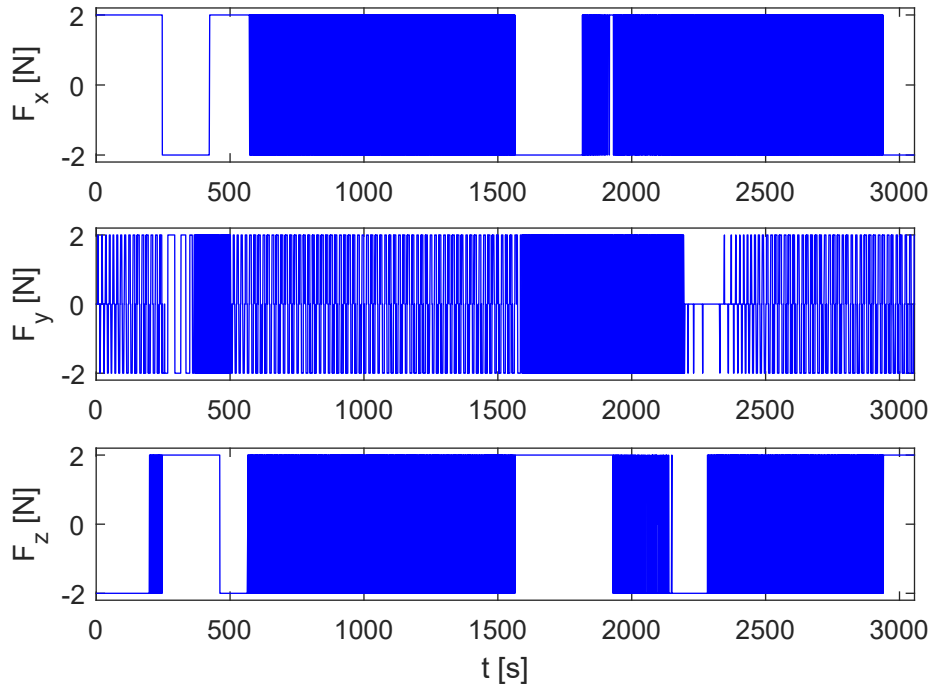
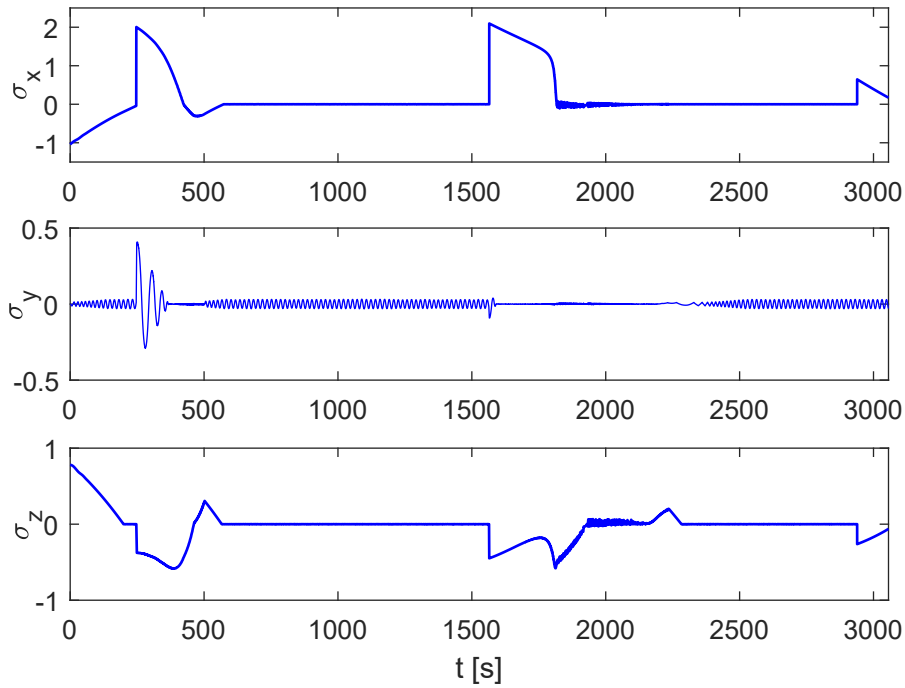


**Figure 6.10:** Forces of the thrusters during radial boost

The forces exerted by the thrusters are shown in Figure 6.10. It can be seen that the constraint to the maximum value is respected. For the duration of the maneuver  $F_y$  swings from positive to negative to keep  $y = 0$ .

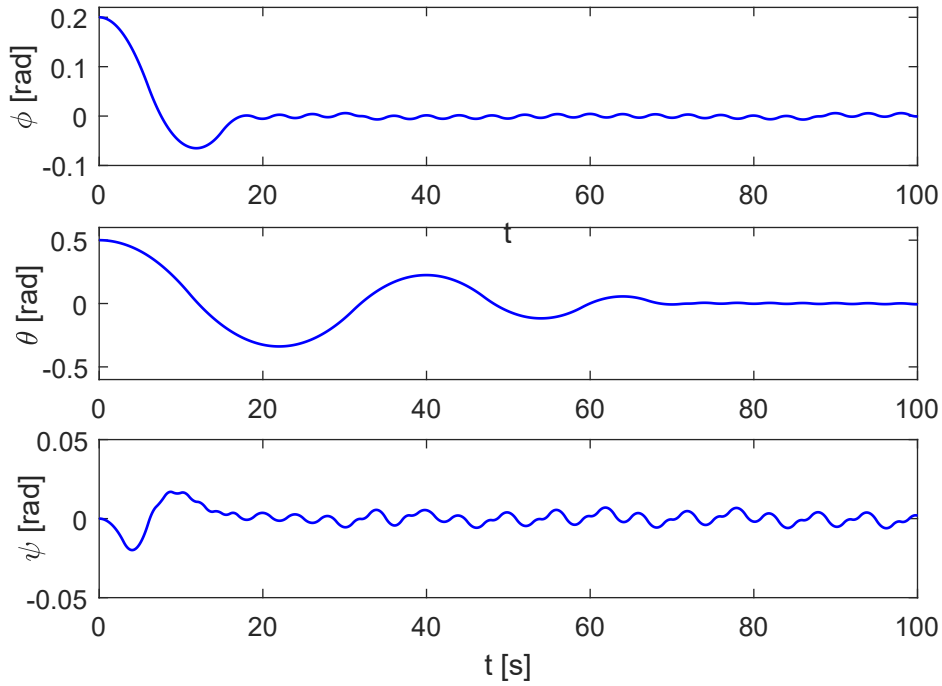
At the early stages of the maneuver  $F_z$  assumes a negative value to adjust the initial value of  $v_z$  that tends to draw Chaser away from  $z = 0$ , while  $F_x$  is greater than zero to increase the value of  $v_x$ .

Approximately at  $t = 250$  s  $F_x$  becomes negative to reduce the component of the velocity of the Chaser direct toward the obstacle, while  $F_z$  is positive to allow the circumvention of the obstacle. This also occurs in proximity of the second obstacle. Towards the end of the maneuver  $F_x$  has a negative value to ensure the reduction of the desired speed imposed by the guidance algorithm.



**Figure 6.11:** Sliding surfaces of the guidance control during radial boost

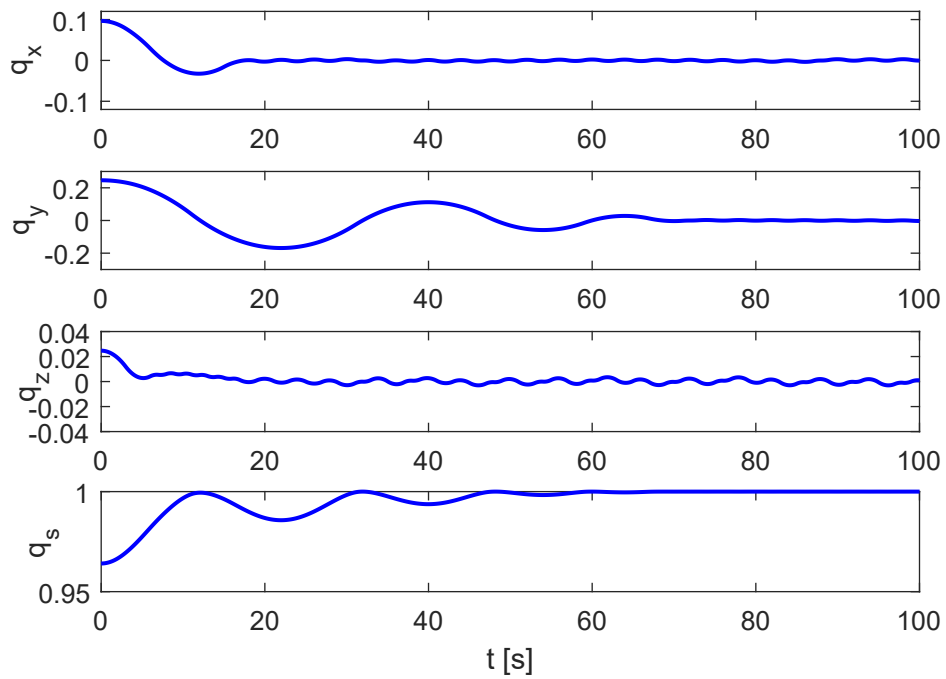
Figure 6.11 provides the sliding surface of the sliding mode control for the position dynamics. All three components tend to zero, this indicates a good behavior of the control law. The  $x$  and  $z$  components suffer deviations in the proximity of obstacles, while the step towards the end of the maneuver is due to the change of the desired speed. Later, values tend back to zero. Instead,  $\sigma_y$  fluctuates around zero for most of the maneuver, its amplitude of oscillation is in the order of  $10^{-2}$ , whereas the amplitude of  $\sigma_x$  and  $\sigma_z$  is 3 order of magnitude lower.



**Figure 6.12:** The Euler angles during radial boost

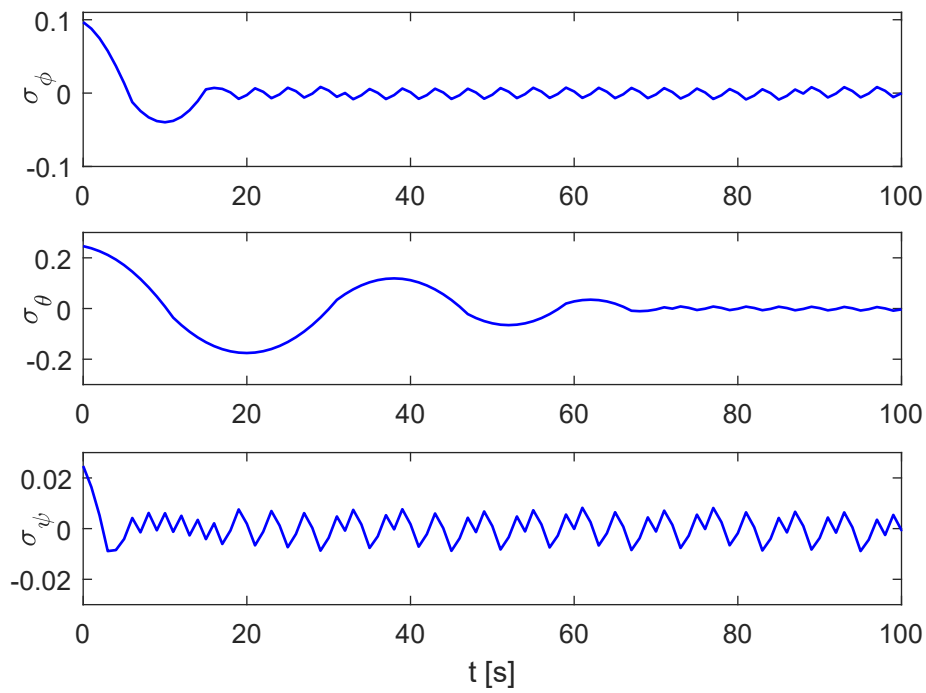
The graphs of the attitude are shown for the first 100 seconds of the maneuver because within this time the initial values of the quaternions converge to the desired ones by means of the control system and for the rest of the maneuver parameters oscillate around the values achieved by maintaining this attitude.

At the beginning the  $F_a$  frame is rotated against  $F_{lo}$ , so the attitude of the Chaser is not the desired one. As Figure 6.12 shows, the control system is able to achieve the desired attitude within 20 seconds in terms of  $\phi$ , and in about 70 seconds in terms of  $\theta$ . Instead, the value of  $\psi$  is already the desired one when the maneuver starts. Since the angles arrive to convergence, they fluctuate around the desired values, with amplitude of about  $10^{-3}$  deg.



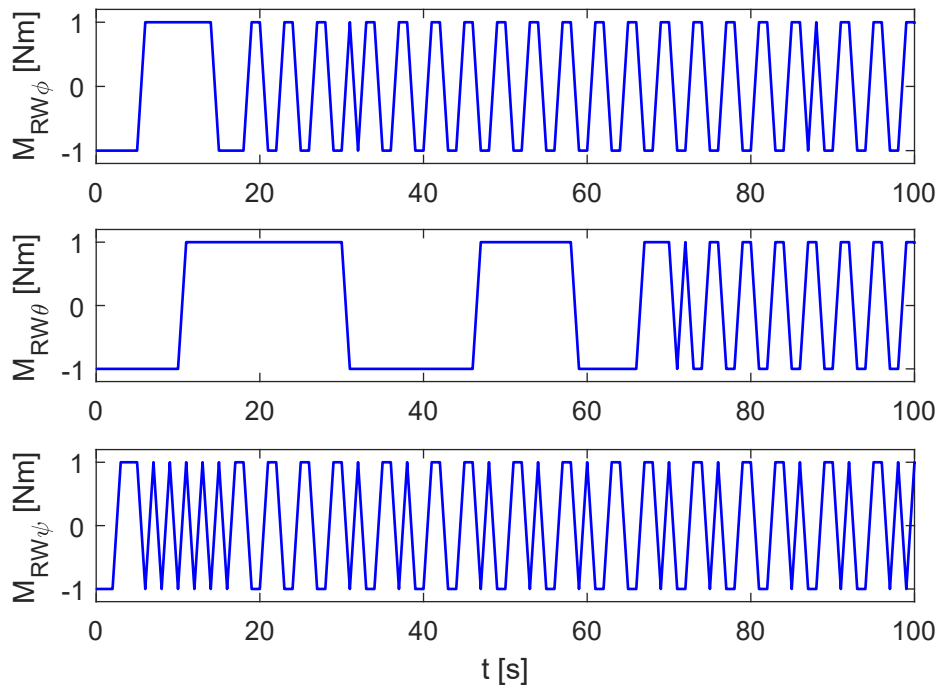
**Figure 6.13:** The quaternions during radial boost

The development of quaternions, shown in Figure 6.13, also confirm that the attitude of the Chaser go to convergence in about 70 seconds, and after the amplitude of the fluctuations is of the order of  $10^{-3}$ .



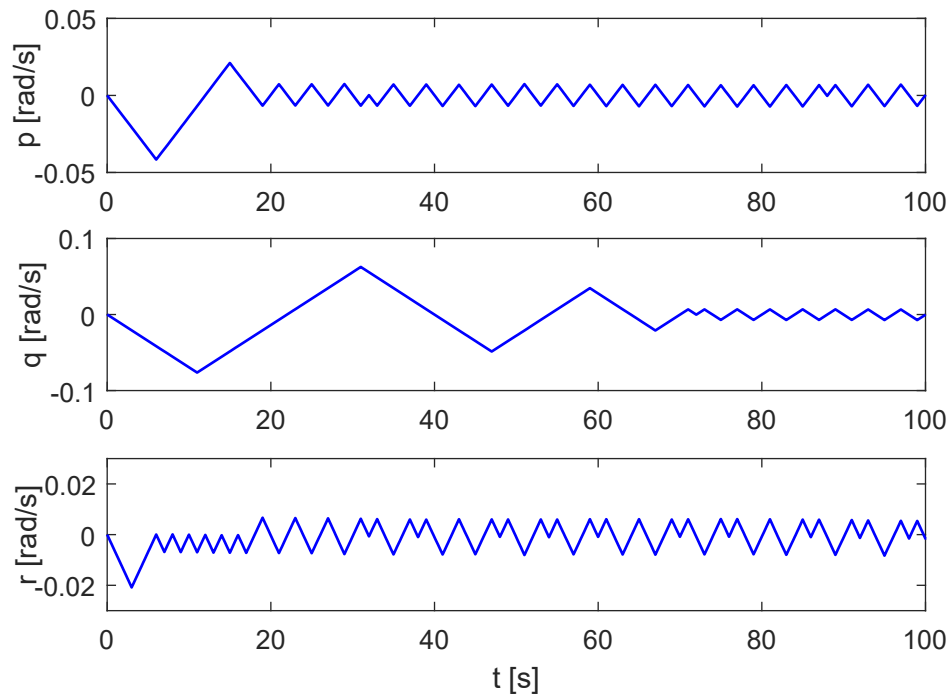
**Figure 6.14:** Sliding surfaces of the attitude control during radial boost

Figure 6.14 provide the component of the sliding surface. The evolution over time confirm the values of the time needed to achieve convergence in terms of  $\phi$ ,  $\theta$  and  $\psi$ . In the latter figure the chattering phenomenon can be observed. In fact the output of the controller oscillates around zero, with an amplitude of about  $10^{-2}$ . This value can be decreased by increasing the frequency of the attitude control.



**Figure 6.15:** Torques provided by reaction wheels during radial boost

Figure 6.15 shows the moment provided by the reaction wheels. The saturation value is respected and the period of the oscillation is longer until convergence is reached. After the fluctuations are more frequent in order to maintain the desired attitude.

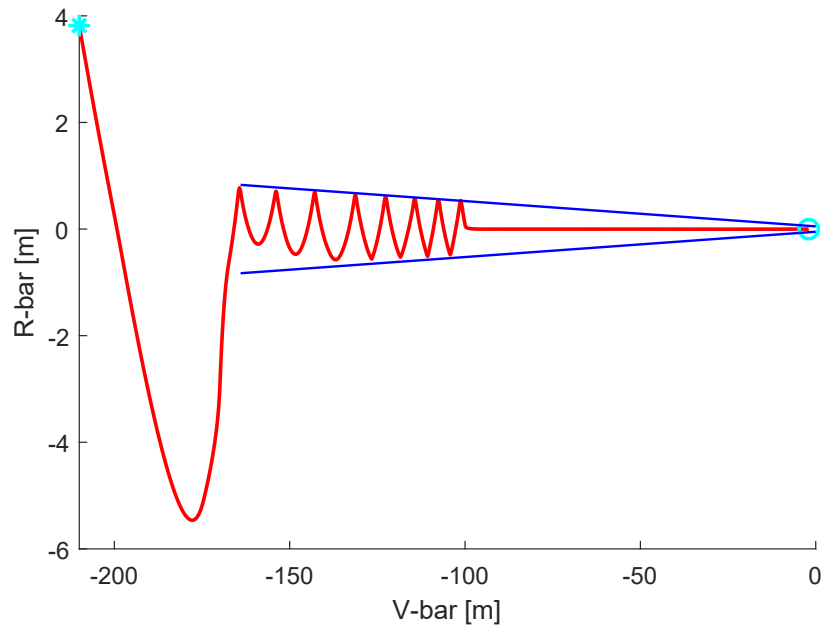


**Figure 6.16:** Rotation speeds during radial boost

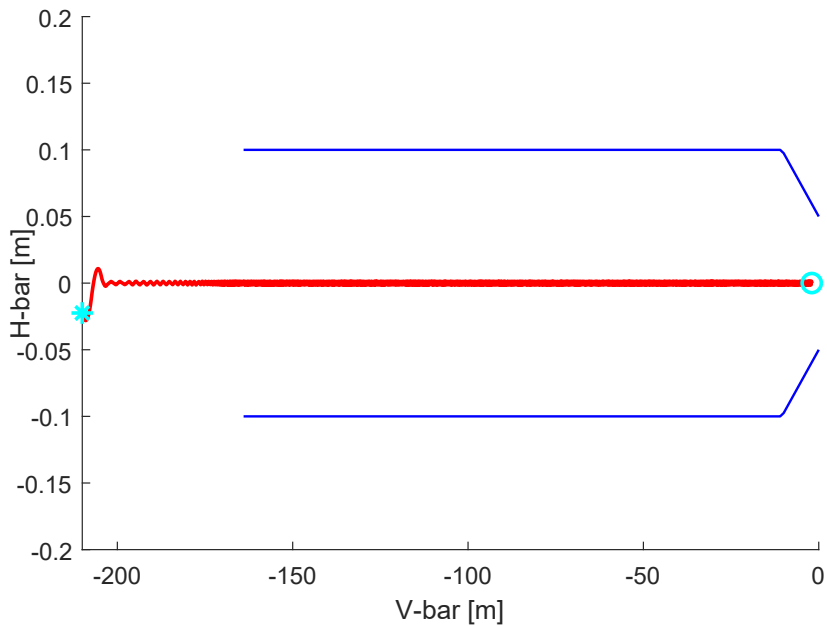
Figure 6.16 provides the rotation speeds of the chaser. They also fluctuate once the spacecraft has reached the desired attitude, with the same values of the order of  $10^{-3}$ .

### 6.3.2 The cone approach

This section provides the same graphs of subsection 6.3.1, but related to the cone approach.

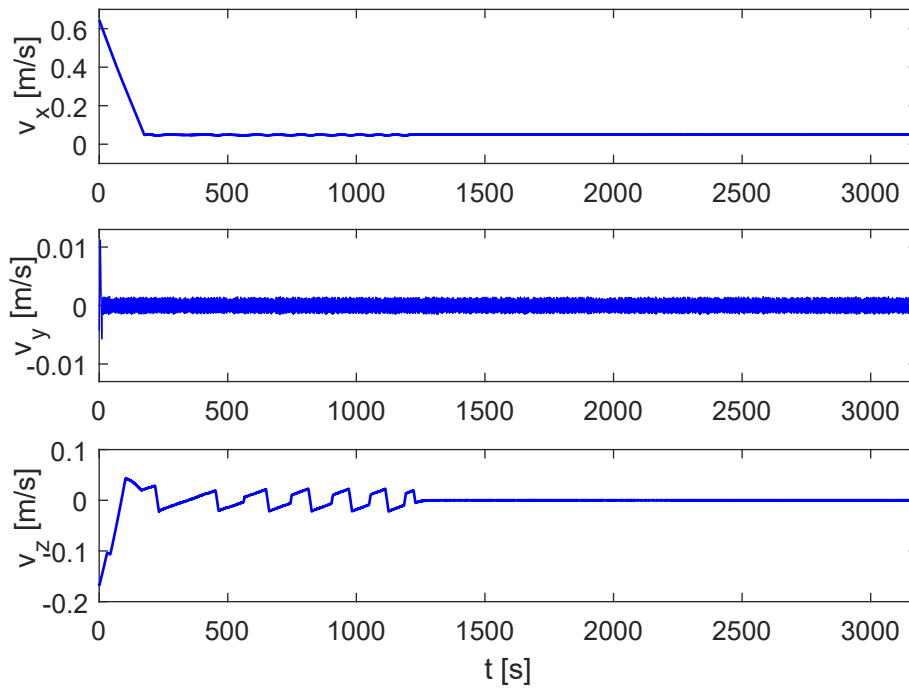


**Figure 6.17:** Trajectory of the chaser in the  $xz$  plane during final approach



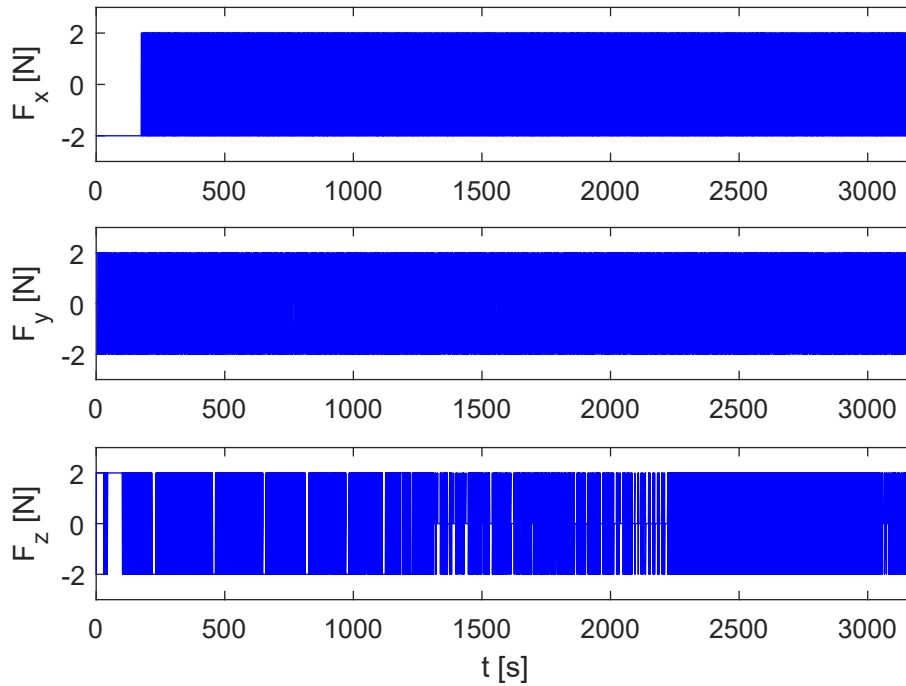
**Figure 6.18:** Trajectory of the chaser in the  $xy$  plane during final approach

Figure 6.17 shows that the chaser is able to get into the cone after the end of the Radial Boost, then it makes a trajectory at half-waves in the  $xz$  plane during the first part of the cone, and it finishes at  $x = -2$  m from the target with a straight-line approach. Instead, Figure 6.18 shows that the  $y$  coordinate oscillates around zero, within the limits set. The guidance and control algorithm has a high accuracy since that at the end of the maneuver the error in  $R$ -bar is  $10^{-5}$  m and  $10^{-4}$  m along  $H$ -bar. For the final approach, calculated consumption is 5.75 kg of propellant.



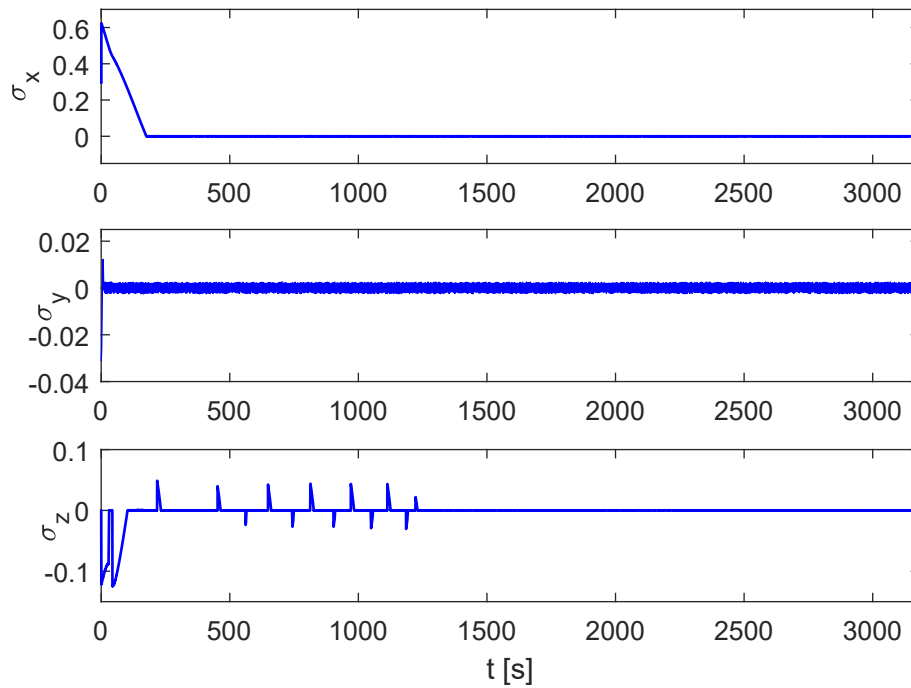
**Figure 6.19:** Speed during final approach

Figure 6.19 shows that initially the value of  $v_x$  drops, and then remain constant at  $0.05 \text{ m/s}$ . In the first part of the trajectory,  $v_z$  ranges from zero to a non-zero value, which is taken when the satellite must push along  $z$  to remain inside the cone. While during the straight-line approach  $v_z$  is approximately zero, as well as  $v_y$ , except for the oscillations of  $10^{-3} \text{ m/s}$ .



**Figure 6.20:** Forces during final approach

As it can be seen in Figure 6.20 the values of the force  $F_y$  oscillates during all the cone to maintain the desired position  $y = 0$ . Instead, in the first phase,  $F_x$  takes a negative value to decelerate the satellite, which has a speed  $v_x$  too high, then it fluctuates to maintain the desired speed  $v_x = 0.05 \text{ m/s}$ .  $F_z$  oscillates too, in order to maintain the satellite within the cone.



**Figure 6.21:** Sliding surfaces of the guidance control during final approach

The sliding surface of the sliding mode control for position is in Figure 6.21. In this maneuver, as in the previous, all three components tend to zero and the amplitude of the fluctuations of the sliding output are about  $10^{-3}$ . For the reasons explained in Subsection 6.3.1 the graphs related to the attitude are not shown for this phase, the error in terms of quaternions is in the order of  $10^{-4}$  at the end of the maneuver.

# Chapter 7

## Conclusions

The main objective of this thesis was to analyze the effectiveness of the APF method combined with SMC to achieve an autonomous rendezvous maneuver. For this purpose, guidance and control algorithms have been designed in the Matlab software, where the nonlinear orbital dynamic is included.

In particular, through the integration of the Hill equations, the acceleration, speed and position vectors relative to the target are obtained. Within these equations, the forces due to both orbital disturbances and thrusters are included. The first are estimated based on physical and orbital characteristics of the Chaser, instead the latter are calculated by the first-order SMC. This has the task of tracking the path planned by the guidance algorithm based on APF. It plans a trajectory *on-line*, based on the goal location and on data about position and speed of Chaser and obstacles.

Instead, through Euler's mathematical method, attitude dynamic has been analyzed, obtaining the orientation of the Chaser. This is controlled through Super-Twisting SMC, that computes the moment which has to be exerted by reaction wheels, in order to overcome the external disturbances and to orient the Chaser. Data on the attitude of the latter are used to rotate the forces applied by the thrusters from body frame to LVLH frame.

Results of the simulations show that APF is an excellent method to plan safety orbital trajectories, whereas SMC is well to track these trajectories, since, in this case study the Chaser is able to approach the Target, respecting the requirements and avoiding obstacle. Despite the many advantages of this strategy to achieve autonomous rendezvous maneuver, such as the effectiveness and the simplicity of implementation, it presents some problematic aspects. As regards the APF method, a crucial weakness is due to the *local minimum*. This situation occurs when the attractive potential and the repulsive one are perfectly equal, as a consequence the gradient of the potential is null and the spacecraft gets trapped in this point of local minimum, therefore the path cannot be completed. Instead, the weakness of the adopted control strategy is the continuous switch between a rule of decision and another. This may generate high-frequency oscillations due to a not perfect sliding along the surface. This phenomenon, known as chatter, is perhaps the only reason that restricts the use of sliding mode control: these annoying vibrations can

degrade components much faster, increasing the probability of failure.

In this thesis, the obstacles had a spherical geometry and it was assumed that the initial position of their center were known. In reality, the space debris are often shaped like ellipsoid, this can be taken into account in possible future works. Another aspect to be discussed concerns the gains of the APF, which play an important role in the formulation of attractive and repulsive force. In this work,  $k_a$  and  $k_r$  were obtained by trial to ensure tracking and obstacle avoidance. The algorithm can be improved by adding an additional algorithm that allows adjusting these parameters automatically, depending on the size of the obstacle and the relative speed.

# Chapter 8

## Appendix

### 8.1 Matlab script

---

```
clear;
clc;

m_c0 = 600;
m_c=m_c0;

lx    = 1.2;
ly    = 1.2;
lz    = 1.2;
Jx0=(m_c0*(2*lx^2)/12);
Jy0=(m_c0*(2*ly^2)/12);
Jz0=(m_c0*(2*lz^2)/12);
I_b0=[Jx0  0  0;
       0  Jy0  0;
       0  0  Jz0];

mu=3.986012*10^14;
r_t=6378.145*10^3;
height=500000;
r=r_t+height;
om=(mu/r^3)^0.5;
x_f_r=-200;
x_i_r=-3000;
Vz_i_r=om/4*(x_f_r-x_i_r);

Tmax=1;
n=2;
tau_z=50;
```

```
gamma_z=om*(x_f_r-x_i_r)/4/tau_z;
```

```
Isp=220;
```

```
g0=9.806;
```

```
m_c_dot=n*Tmax/g0/Isp;
```

```
rho = 1*10^(-12);
```

```
Vx = om*r;
```

```
CD = 2.2;
```

```
A = ly*lz;
```

```
F_D = 1/2*rho*CD*A*Vx^2;
```

```
F_D = [F_D 0 0];
```

```
F_SP=10^-7*[1;1;1];
```

```
M_grav=10^-3*[1;1;1];
```

```
M_SP=10^-6*[1;1;1];
```

```
M_thr=[0;0;0];
```

```
F_thr=[0;0;0];
```

```
Ax=0;
```

```
Ay=0;
```

```
Az=0;
```

```
t_filtro_x=0;
```

```
t_filtro_y=0;
```

```
t_filtro_z=0;
```

```
RC=0.001;
```

```
Ka=100;
```

```
Kr=1000000;
```

```
eta_0=300;
```

```
raggio=50;
```

```
eta_0=eta_0+raggio;
```

```
pos_OBS_R_1=[-2400 100 15];
```

```
vel_OBS_R_1=[-0.5 -0.08 0.02];
```

```
pos_OBS_R_2=[-1430 -50 -500];
```

```
vel_OBS_R_2=[0.15 0.02 0.3];
```

```
pos_FIN_R=[-200 0 0];
```

```
c=[0 0 0;
```

```
0 1 0;
```

```
0 0 0];
```

```
entrata_iniziale_STW=1;
```

```
entrata_iniziale_APF=1;
```

```
entrata_iniziale_SMC=1;
cont_SMC=0;
cont_APF=0;
cont_STW=0;
cont_t_morto_1=0;
cont_t_morto_2=0;
cont_t_morto_3=0;
cont_banda_vuota_1=0;
cont_banda_vuota_2=0;
cont_banda_vuota_3=0;
j=1;
tt=1;
t_smc=0;
ttt=1;
t_stw=0;
avvertimento_ostacolo_1=0;
avvertimento_ostacolo_2=0;

omega_b=[0;0;0];
I_RW=0.1*eye(3,3);
M_RW=[0;0;0];
omega_RW=[0;0;0];
omega_dot_RW=[0;0;0];
M_B=M_RW;
I_b=I_b0;

eul_ang0 = [0.2,0.5,0];
q_func=angle2quat(0.2, 0.5, 0, 'XYZ');
q(1)=q_func(2);
q(2)=q_func(3);
q(3)=q_func(4);
q(4)=q_func(1);
q0=q;
q=q';
var_q=q;
q_des=[0;0;0;1];
Q13_des=[0 -q_des(3) q_des(2);
          q_des(3) 0 -q_des(1);
          -q_des(2) q_des(1) 0];
SIGMA_q_des=[q_des(4)*eye(3,3)+Q13_des;
              -q_des(1:3)'];

M_RW_MAX=1;
Lambda = eye(3,3);
```

```
C1 = 0.2;
C2 = 0.3;
C3 = 0.3;

UM1 = 600;
UM2 = 400;
UM3 = 400;

Km = 0.005;
KM = 0.01;

qu = 0.5;
alpha = 1;

lambda1 = 1.1*sqrt(2/abs(Km*alpha-C1))*((Km*alpha+C1)*
      KM*(1+qu))/(Km^2*(1-qu));
lambda2 = 1.1*sqrt(2/abs(Km*alpha-C2))*((Km*alpha+C2)*
      KM*(1+qu))/(Km^2*(1-qu));
lambda3 = 1.1*sqrt(2/abs(Km*alpha-C3))*((Km*alpha+C3)*
      KM*(1+qu))/(Km^2*(1-qu));

v1=0.001;
v2=0.001;
v3=0.001;

num_it_max=700000;
x_free_fligth=zeros(1,num_it_max);
z_free_fligth=zeros(1,num_it_max);
y_free_fligth=zeros(1,num_it_max);
pos_OBS_R_1_vett=zeros(num_it_max/100,3);
pos_OBS_R_2_vett=zeros(num_it_max/100,3);
vel_x=zeros(1,num_it_max);
vel_y=zeros(1,num_it_max);
vel_z=zeros(1,num_it_max);
t_plot=zeros(1,num_it_max);
omega_p=zeros(1,num_it_max);
omega_q=zeros(1,num_it_max);
omega_r=zeros(1,num_it_max);
q1_plot=zeros(1,num_it_max);
q2_plot=zeros(1,num_it_max);
q3_plot=zeros(1,num_it_max);
q4_plot=zeros(1,num_it_max);
phi=zeros(1,num_it_max);
thetaa=zeros(1,num_it_max);
```

```
psi=zeros(1,num_it_max);
sigma_plot_stw_x=zeros(1,num_it_max/100);
sigma_plot_stw_y=zeros(1,num_it_max/100);
sigma_plot_stw_z=zeros(1,num_it_max/100);
t_plot_stw=zeros(1,num_it_max/100);
M_RW_x=zeros(1,num_it_max/100);
M_RW_y=zeros(1,num_it_max/100);
M_RW_z=zeros(1,num_it_max/100);
sigma_plot_smc_x=zeros(1,num_it_max/10);
sigma_plot_smc_y=zeros(1,num_it_max/10);
sigma_plot_smc_z=zeros(1,num_it_max/10);
t_plot_smc=zeros(1,num_it_max/10);
F_plot_x=zeros(1,num_it_max);
F_plot_y=zeros(1,num_it_max);
F_plot_z=zeros(1,num_it_max);

x=-inf;
i=1;
num_it=0;

while x<(x_f_r-10) && num_it<num_it_max

    num_it=num_it+1;
    [t,v]=ode45(@ (t,v) hill_new(t,v,Ax,Ay,Az), dt, v0);

    x_free_fligth(i)=v(end,1);
    z_free_fligth(i)=v(end,3);
    y_free_fligth(i)=v(end,2);
    i=i+1;
    x=v(end,1);
    vel_x(i-1)=v(end,4);
    vel_y(i-1)=v(end,5);
    vel_z(i-1)=v(end,6);
    t_plot(i-1)=t_fin-1/100;

    Jx=(m_c*(2*lx^2)/12);
    Jy=(m_c*(2*ly^2)/12);
    Jz=(m_c*(2*lz^2)/12);
    I_b=[Jx 0 0;
         0 Jy 0;
         0 0 Jz];
```

---

```

M_B=M_RW-M_grav-M_SP+M_thr;
omega_dot_b=I_b^-1*(M_B-cross(omega_b,(I_b*omega_b+
    I_RW*omega_RW)));
omega_dot_RW=I_RW^-1*M_RW-omega_dot_b;

[t_omega_b,y_omega_b]=ode45(@(t,var_omega_b) I_b^-1*
(M_B-cross(var_omega_b,(I_b*var_omega_b+I_RW*omega_RW))),
dt, omega_b);
omega_b=y_omega_b(end,:)' ;
omega_p(i-1)=omega_b(1);
omega_q(i-1)=omega_b(2);
omega_r(i-1)=omega_b(3);

[t_omega_RW,y_omega_RW]=ode45(@(t,var_omega_RW)
I_RW^-1*M_RW-omega_dot_b, dt, omega_RW);
omega_RW=y_omega_RW(end,:)' ;

var_q=q;

OM_om=[0 omega_b(3) -omega_b(2) omega_b(1);
    -omega_b(3) 0 omega_b(1) omega_b(2);
    omega_b(2) -omega_b(1) 0 omega_b(3);
    -omega_b(1) -omega_b(2) -omega_b(3) 0];

q_dot=0.5*OM_om*q;

[t_q,y_q]=ode45(@(t,var_q) 0.5*OM_om*var_q, dt, q);
q=y_q(end,:)' ;

q1_plot(i-1)=q(1);
q2_plot(i-1)=q(2);
q3_plot(i-1)=q(3);
q4_plot(i-1)=q(4);

q_prov(1,1)=q(4);
q_prov(1,2)=q(1);
q_prov(1,3)=q(2);
q_prov(1,4)=q(3);

DCM=quat2dcm(q_prov);

R_eul=DCM;

```

---

```

[r1, r2, r3]=dcm2angle(DCM,'XYZ');
phi(i-1)=r1;
thetaa(i-1)=r2;
psi(i-1)=r3;

v0=v(end,:);
dt=[t_fin,t_fin+1/100];
t_fin=t_fin+1/100;
cont_SMC=cont_SMC+1;
cont_APF=cont_APF+1;
cont_STW=cont_STW+1;

if cont_APF>99.5 || entrata_iniziale_APF>0.5

    entrata_iniziale_APF=0;

    F_attr=Ka*[pos_FIN_R(1)-v(end,1);pos_FIN_R(2)-
v(end,2);pos_FIN_R(3)-v(end,3)];

    pos_OBS_R_1_vett(j,:)=pos_OBS_R_1+vel_OBS_R_1*
(t_fin-2/100-tau_z);
    dist_cha_obs_1=norm(pos_OBS_R_1_vett(j,:)-
v(end,1:3),2);
    dist_cha_obs_1_vett=pos_OBS_R_1_vett(j,:)-
v(end,1:3);
    dist_cha_obs_1_vers=dist_cha_obs_1_vett'/
norm(dist_cha_obs_1_vett,2);
    v_rel_1=(v(end,4:6)-vel_OBS_R_1)*
dist_cha_obs_1_vers;

    a_max=norm(n*Tmax*[1 1 1]/m_c/(2^0.5),2);

    if dist_cha_obs_1<=eta_0 && v_rel_1>0

        if avvertimento_ostacolo_1<0.5
            ing_ob_1=j;
            ing_ob_1_x=i;
            avvertimento_ostacolo_1=1;
        end

        R_dyn_1=eta_0+v_rel_1^2/2/a_max;

        F_rep_1_A=-(-Kr/dist_cha_obs_1^2*(1/dist_cha_obs_1
-1/R_dyn_1)+Kr/(1/dist_cha_obs_1-1/R_dyn_1)/

```

```

R_dyn_1^2*v_rel_1/a_max)*dist_cha_obs_1_vers;

F_rep_1_B=-Kr*(1/dist_cha_obs_1-1/R_dyn_1)/R_dyn_1^2
/(-dist_cha_obs_1)*v_rel_1/a_max*(v(end,4:6)'
-vel_OBS_R_1'-v_rel_1*dist_cha_obs_1_vers);
else

F_rep_1_A=[0;0;0];
F_rep_1_B=[0;0;0];

if avvertimento_ostacolo_1==1
    exit_ob_1=j;
    exit_ob_1_x=i;
    avvertimento_ostacolo_1=0;
end
end

pos_OBS_R_2_vett(j,:)=pos_OBS_R_2+vel_OBS_R_2*
(t_fin-2/100-tau_z);
dist_cha_obs_2=norm(pos_OBS_R_2_vett(j,:)-
v(end,1:3),2);
dist_cha_obs_2_vett=pos_OBS_R_2_vett(j,:)-
v(end,1:3);
dist_cha_obs_2_vers=dist_cha_obs_2_vett'/
norm(dist_cha_obs_2_vett,2);
v_rel_2=(v(end,4:6)-vel_OBS_R_2)*
dist_cha_obs_2_vers;

if dist_cha_obs_2<=eta_0 && v_rel_2>0

if avvertimento_ostacolo_2<0.5
    ing_ob_2=j;
    ing_ob_2_x=i;
    avvertimento_ostacolo_2=1;
end

R_dyn_2=eta_0+v_rel_2^2/2/a_max;

F_rep_2_A=-(-Kr/dist_cha_obs_2^2*(1/dist_cha_obs_2
-1/R_dyn_2)+Kr/(1/dist_cha_obs_2-1/R_dyn_2)/
R_dyn_2^2*v_rel_2/a_max)*dist_cha_obs_2_vers;

F_rep_2_B=-Kr*(1/dist_cha_obs_2-1/R_dyn_2)/R_dyn_2^2
/(-dist_cha_obs_2)*v_rel_2/a_max*(v(end,4:6)'-

```

```
    vel_OBS_R_2' -v_rel_2*dist_cha_obs_2_vers);  
else  
  
    F_rep_2_A=[0;0;0];  
    F_rep_2_B=[0;0;0];  
  
    if avvertimento_ostacolo_2==1  
        exit_ob_2=j;  
        exit_ob_2_x=i;  
        avvertimento_ostacolo_2=0;  
    end  
end  
  
    j=j+1;  
    F_tot=F_attr+F_rep_1_A+F_rep_1_B+F_rep_2_A+F_rep_2_B;  
    EU=F_tot/norm(F_tot,2);  
  
    if x<-300  
        v_max_d=1.4*Vz_i_r*EU;  
    else  
        v_max_d=0.5*Vz_i_r*EU;%0.1*  
    end  
  
    if cont_APF>99.5  
        cont_APF=0;  
    end  
end  
  
    if cont_STW>99.5 || entrata_iniziale_STW>0.5  
  
        delta_q13=SIGMA_q_des'*q;  
        sigma_STW=omega_b+Lambda*delta_q13;  
  
        if entrata_iniziale_STW>0.5  
  
            sigma_plot_stw_x(1)=sigma_STW(1);  
            sigma_plot_stw_y(1)=sigma_STW(2);  
            sigma_plot_stw_z(1)=sigma_STW(3);  
            t_plot_stw(1)=0;  
        end  
  
        if entrata_iniziale_STW<0.5  
            ttt=ttt+1;  
            t_stw=t_stw+1;  
        end
```

---

```

        sigma_plot_stw_x(ttt)=sigma_STW(1);
        sigma_plot_stw_y(ttt)=sigma_STW(2);
        sigma_plot_stw_z(ttt)=sigma_STW(3);
        t_plot_stw(ttt)=t_stw;
    end

    entrata_iniziale_STW=0;

    [t_v1,y_v1]=ode45(@ (t,var_v_dot)
    -alpha*sign(sigma_STW(1)), [0 1], v1);
    v1=y_v1(end);

    [t_v2,y_v2]=ode45(@ (t,var_v_dot)
    -alpha*sign(sigma_STW(2)), [0 1], v2);
    v2=y_v2(end);

    [t_v3,y_v3]=ode45(@ (t,var_v_dot)
    -alpha*sign(sigma_STW(3)), [0 1], v3);
    v3=y_v3(end);

    M_RW(1,1)=-lambda1*(abs(sigma_STW(1)))^0.5
    *sign(sigma_STW(1))+v1;
    M_RW(2,1)=-lambda2*(abs(sigma_STW(2)))^0.5
    *sign(sigma_STW(2))+v2;
    M_RW(3,1)=-lambda3*(abs(sigma_STW(3)))^0.5
    *sign(sigma_STW(3))+v3;

    M_RW_nominale_x(ttt)=M_RW(1);
    M_RW_nominale_y(ttt)=M_RW(2);
    M_RW_nominale_z(ttt)=M_RW(3);

    for p=1:3
        if M_RW(p) > M_RW_MAX
            M_RW(p) = M_RW_MAX;
        elseif M_RW(p) < -M_RW_MAX
            M_RW(p) = -M_RW_MAX;
        end
    end

    M_RW_x(ttt)=M_RW(1);
    M_RW_y(ttt)=M_RW(2);
    M_RW_z(ttt)=M_RW(3);

    if cont_STW>99.5

```

```
        cont_STW=0;
    end
end

    if cont_SMC>9.5 || entrata_iniziale_SMC>0.5

sigma=(v(end,4:6)'-v_max_d)+
c*(v(end,1:3)'-pos_FIN_R');
F_thr_des=-n*Tmax*sign(sigma);

    if entrata_iniziale_SMC>0.5

        sigma_plot_smc_x(1)=sigma(1);
        sigma_plot_smc_y(1)=sigma(2);
        sigma_plot_smc_z(1)=sigma(3);
        t_plot_smc(1)=0;
    end

    if entrata_iniziale_SMC<0.5
        tt=tt+1;
        t_smc=t_smc+1/10;
        sigma_plot_smc_x(tt)=sigma(1);
        sigma_plot_smc_y(tt)=sigma(2);
        sigma_plot_smc_z(tt)=sigma(3);
        t_plot_smc(tt)=t_smc;
    end

    if abs(v(end,2)-pos_FIN_R(2))<10^-2
        F_thr_des(2)=0;
    end

    if cont_SMC>9.5
        cont_SMC=0;
    end
end

t_filtro_x=t_filtro_x+1/100;
t_filtro_y=t_filtro_y+1/100;
t_filtro_z=t_filtro_z+1/100;

if cont_SMC<1.5 && (sign(F_thr_des(1))~=sign(F_thr(1)))
|| F_thr_des(1)==0 && entrata_iniziale_SMC<0.5
    F_thr(1)=0;
    t_filtro_x=0;
```

```

else
    F_thr(1)=F_thr_des(1);
end

if cont_SMC<1.5 && (sign(F_thr_des(2))~=sign(F_thr(2))
|| F_thr_des(2)==0) && entrata_iniziale_SMC<0.5

    F_thr(2)=0;
    t_filtro_y=0;
else
    F_thr(2)=F_thr_des(2);
end

if cont_SMC<1.5 && (sign(F_thr_des(3))~=sign(F_thr(3))
|| F_thr_des(3)==0) && entrata_iniziale_SMC<0.5

    F_thr(3)=0;
    t_filtro_z=0;
else
    F_thr(3)=F_thr_des(3);
end

n=0;
if F_thr(1)~=0
    n=n+2;
end
if F_thr(2)~=0
    n=n+2;
end
if F_thr(3)~=0
    n=n+2;
end

[t_m_c,y_m_c]=ode45(@(t,var_m_c)
-n*Tmax/g0/Isp, dt-1/100, m_c);
m_c=y_m_c(end);
n=2;

F_filtro(1,1)=F_thr(1)*(1-exp(-t_filtro_x/RC));
F_filtro(2,1)=F_thr(2)*(1-exp(-t_filtro_y/RC));
F_filtro(3,1)=F_thr(3)*(1-exp(-t_filtro_z/RC));
[F_vera,M_thr]=erth_mag(F_filtro,lx,ly,lz);
F_vera_rot=R_eul*F_vera;

```

```
J2x=normrnd(0,10^-6,1,1);
J2y=normrnd(0,10^-6,1,1);
J2z=normrnd(0,10^-6,1,1);
F_J2=[J2x J2y J2z]';

F_vera_tot=F_vera_rot-F_D'+F_J2+F_SP;
acc=F_vera_tot/m_c;

F_plot_x(i-1)=F_filtro(1);
F_plot_y(i-1)=F_filtro(2);
F_plot_z(i-1)=F_filtro(3);

Ax=acc(1);
Ay=acc(2);
Az=acc(3);

entrata_iniziale_SMC=0;
end

m_c_rad=m_c;
t_in_cono=t_fin-1/100;
num_it_cono=0;
tt=1;
t_smc=0;
ttt=1;
t_stw=0;
```

---

For the cone of approach this algorithm is repeated, but the cycle related to APF is different:

---

```
pos_FIN_D=[-2 0 0];
v_max=0.05;
d1 = 200;
d1_in=150;
rc1 = 1;
rc2 = 0.05;
a = sqrt(d1^2 + (rc1 - rc2)^2);
teta = atan((rc1 - rc2)/d1);

if cont_APF>99.5 || entrata_iniziale_APF>0.5

    entrata_iniziale_APF=0;

    if x<-d1/2+50
        F_attr=Ka*[pos_FIN_D(1)-v(end,1);pos_FIN_D(2)-v(end,2);
        100*(pos_FIN_D(3)-v(end,3))];%*100z
```

```
else
    F_attr=Ka*[pos_FIN_D(1)-v(end,1);pos_FIN_D(2)-v(end,2);
    pos_FIN_D(3)-v(end,3)];
end

F_tot=F_attr;
EU=F_tot/norm(F_tot,2);

v_max_d=v_max*EU;

if x<-d1_in
    if v(end,3)<(-teta*(-d1_in)+rc2)*0.85 &&
    v(end,3)>(teta*(-d1_in)-rc2)*0.85
        v_max_d(3)=v(end,6);
    end
end

if x>-d1_in && x<-d1/2
    if v(end,3)<(-teta*x+rc2)*0.85 && v(end,3)>(teta*x-rc2)*0.85
        v_max_d(3)=v(end,6);
    end
end

if cont_APF>99.5
    cont_APF=0;
end
end
```

---

# Bibliography

- [1] Yazhong L., Jin Z., Guojin T., Survey of orbital dynamics and control of space rendezvous, Chinese Journal of Aeronautics, 2014;
- [2] Fehse, W., Automated Rendezvous and Docking of Spacecraft, New York: Cambridge University Press, 2003;
- [3] Lu P., Liu X., Autonomous Trajectory Planning for Rendezvous and Proximity Operations by Conic, Journal of Guidance Control and Dynamics Optimization, 2013;
- [4] Orbital Debris Management and Risk Mitigation, Nation Aeronautics and Space Administration, Accademy of Program/Project and Engineering Leadership;
- [5] Corpino S., Dispense del Corso di Sistemi aerospaziali, Politecnico di Torino, 2016/2017
- [6] Dentis M., Capello E., Guglieri G., A novel concept for guidance and control of spacecraft orbital maneuvers, International Journal of Aerospace Engineering, 2016;
- [7] Capello E., Punta E., Dabbene F., Guglieri G., Tempo R., Sliding Mode Control strategies for rendezvous and docking maneuvers, Journal of Guidance, Control, and Dynamics, 2017;
- [8] Grojèkatthöfer K., Yoon Z., Introduction into quaternions for spacecraft attitude representation, Department of Astronautics and Aeronautics, Berlino, 2012;
- [9] De Luca A., Dispense Corso di Robotica 2, Pianificazione del moto tra gli ostacoli, Università degli studi di Roma "Sapienza", 2008-2009;
- [10] Pallottino L., Dispense Corso di Sistemi Robotici Distribuiti, Research Center "E. Piaggio", Università di Pisa, 2015;
- [11] Safadi H., Local Path Planning Using Virtual Potential Field, McGill University School of Computer Science, Tech. Rep., 2007;
- [12] Kuipers B. Lectur 7,CS 344R:Robotics, Potential Fields and Model Predictive Control;

- [13] Guldner, J. and Utkin, V. I., "Sliding Mode Control for Gradient tracking and Robot Navigation using Artificial Potential Fields," IEEE Transactions on Robotics and Automation, vol. 11, no. 2, pp. 247-254, 1995;
- [14] S.S. GE, Y.J. CUI, Dynamic Motion Planning for Mobile Robots Using Potential Field Method, Autonomous Robots, 2002;
- [15] Mendes M.F., Kraus W., De Pieri E.R., Variable structure position control of an industrial robotic manipulator, Journal of the Brazilian Society of Mechanical Sciences, 2002;
- [16] Shtessel Y., Edwards C., Fridman L., Levant A., Sliding Mode Control and Observation, 2013
- [17] F. Landis Markley, John L. Crassidis, Fundamentals of Spacecraft Attitude Determination and Control, 2014